ARCHIVIO ISTITUZIONALE DELLA RICERCA

Alma Mater Studiorum Università di Bologna
Archivio istituzionale della ricerca

Systematic Study on the Absorption Features of Interstellar Ices in the Presence of Impurities

This is the final peer-reviewed author's accepted manuscript (postprint) of the following publication:

Published Version:
Systematic Study on the Absorption Features of Interstellar Ices in the Presence of Impurities / Gorai P.; Sil M.; Das A.; Sivaraman B.; Chakrabarti S.K.; Ioppolo S.; Puzzarini C.; Kanuchova Z.; Dawes A.; Mendolicchio M.; Mancini G.; Barone V.; Nakatani N.; Shimonishi T.; Mason N.. - In: ACS EARTH AND SPACE CHEMISTRY. - ISSN 2472-3452. - STAMPA. - 4:6(2020), pp. 920-946. [10.1021/acsearthspacechem.0c00098]

Availability:
This version is available at: https://hdl.handle.net/11585/783283 since: 2020-12-04

Published:

DOI: http://doi.org/10.1021/acsearthspacechem.0c00098

Terms of use:

Some rights reserved. The terms and conditions for the reuse of this version of the manuscript are specified in the publishing policy. For all terms of use and more information see the publisher's website.

This item was downloaded from IRIS Università di Bologna (https://cris.unibo.it/).
When citing, please refer to the published version.

(Article begins on next page)

03 May 2024

This is the final peer-reviewed accepted manuscript of:

P. Gorai, M. Sil, A. Das, B. Sivaraman, S. K. Chakrabarti, S. Ioppolo, C. Puzzarini, Z. Kanuchova, A. Dawes, M. Mendolicchio, G. Mancini, V. Barone, N. Nakatani, T. Shimonishi, N. Mason. Systematic Study on the Absorption Features of Interstellar Ices in the Presence of Impurities. ACS Earth Space Chem. 4 (2020) 920

The final published version is available online at:
https://doi.org/10.1021/acsearthspacechem.0c00098

Terms of use:

Some rights reserved. The terms and conditions for the reuse of this version of the manuscript are specified in the publishing policy. For all terms of use and more information see the publisher's website.

This item was downloaded from IRIS Università di Bologna (https://cris.unibo.it/)

When citing, please refer to the published version.

A Systematic Study on the Absorption Features of Interstellar Ices in Presence of Impurities

P. Gorai,[*,†] M. Sil,[*,†] A. Das,[*,†] B. Sivaraman,[‡] S. K. Chakrabarti,[†] S. Ioppolo,[*,¶,§] C. Puzzarini,[*,‖] Z. Kanuchova,[⊥] A. Dawes,[§] M. Mendolicchio,[#] G. Mancini,[#] V. Barone,[*,#] N. Nakatani,[@,△] T. Shimonishi,[∇,††] and N. Mason[‡‡,§]

†*Indian Centre for Space Physics, 43 Chalantika, Garia Station Road, Kolkata 700084, India*

‡*Atomic Molecular and Optical Physics Division, Physical Research Laboratory, Ahmedabad, India*

¶*School of Electronic Engineering and Computer Science, Queen Mary University of London, Mile End Road, London E1 4NS, UK*

§*Department of Physical Sciences, The Open University, Milton Keynes, UK*

‖*Dipartimento di Chimica Giacomo Ciamician, Via F. Selmi 2, 40126 Bologna, Italy*

⊥*Astronomical Institute of Slovak Academy of Sciences, SK-059 60 Tatranska Lomnica, Slovakia*

#*Scuola Normale Superiore, piazza dei Cavalieri 7, 56125 Pisa, Italy*

@*Institute for Catalysis, Hokkaido University, N21W10 Kita-ku, Sapporo, Hokkaido 001-0021, Japan*

△*Department of Chemistry, Graduate School of Science and Engineering, Tokyo Metropolitan University, 1-1 Minami-Osawa, Hachioji, Tokyo 192-0397, Japan*

∇*Frontier Research Institute for Interdisciplinary Sciences, Tohoku University, Aramakiazaaoba 6-3, Aoba-ku, Sendai, Miyagi, 980-8578, Japan*

††*Astronomical Institute, Tohoku University, Aramakiazaaoba 6-3, Aoba-ku, Sendai, Miyagi, 980-8578, Japan*

‡‡*School of Physical Sciences, University of Kent, Canterbury, Kent, CB2 7NH, United Kingdom*

E-mail: prasanta.astro@gmail.com; milansil93@gmail.com; ankan.das@gmail.com; s.ioppolo@qmul.ac.uk; cristina.puzzarini@unibo.it; vincenzo.barone@sns.it

Abstract

Spectroscopic studies play a key role in the identification and analysis of interstellar ices and their structure. Some molecules have been identified within the interstellar

ices either as pure, mixed or even as layered structures. Absorption band features of water ice can significantly change with the presence of different types of impurities (CO, CO_2, CH_3OH, H_2CO, etc.). In this work, we carried out a theoretical investigation to understand the behavior of water band frequency, and strength in the presence of impurities. The computational study has been supported and complemented by some infrared spectroscopy experiments aimed at verifying the effect of HCOOH, NH_3, and CH_3OH on the band profiles of pure H_2O ice. Specifically, we explored the effect on the band strength of libration, bending, bulk stretching, and free-OH stretching modes. Computed band strength profiles have been compared with our new and existing experimental results, thus pointing out that vibrational modes of H_2O and their intensities can change considerably in the presence of impurities at different concentrations. In most cases, the bulk stretching mode is the most affected vibration, while the bending is the least affected mode. HCOOH was found to have a strong influence on the libration, bending, and bulk stretching band profiles. In the case of NH_3, the free-OH stretching band disappears when the impurity concentration becomes 50%. This work will ultimately aid a correct interpretation of future detailed spaceborne observations of interstellar ices by means of the upcoming JWST mission.

Keywords: Astrochemistry, spectra, ISM: molecules, methods: numerical, experimental, infrared: Band strength, interstellar ice.

1 Introduction

Interstellar grains mainly consist of nonvolatile silicate or carbonaceous compounds covered by icy mantle layers. Interstellar ices play a crucial role in the chemical enrichment of the interstellar medium (ISM). While the existence of interstellar ice was first proposed by Eddington [1] in 1937, a turning point was marked, more than 40 years later, when Tielens and Hagen [2] introduced a combined gas-grain chemistry for the chemical evolution of the ISM. More recently, it has been demonstrated that even pre-biotic molecules can be produced

in UV-irradiated astrophysical relevant ices.[3] For instance, Nuevo et al.[4] experimentally showed that nucleobases can be formed by UV irradiation of pyrimidine in H_2O-rich ice mixtures containing NH_3, CH_3OH, and CH_4.

The composition of interstellar ices can be determined through their absorption spectra in the infrared (IR) region. Since the composition of ISM grain mantles strongly depends on physical conditions,[5–8] the observed spectra can be very different in different astrophysical regions. H_2O is the most dominant ice component in dense molecular clouds,[9] accounting for $60 - 70\%$ of the icy mantels.[10] Water ice was firstly detected through the comparison of ground-based observations of its O-H stretching band at 3278.69 cm^{-1} (3.05 μm) toward Orion-KL[11] and laboratory work by Irvine and Pollack[12]. Since then, several ground-based observations were carried out to identify the signatures of water ice in different astrophysical environments, with further laboratory studies supporting such observations.[13–15] More recently, water was detected by the space-borne Infrared Space Observatory (ISO) mission through its Short-Wavelength Spectrometer (SWS) and Long-Wavelength Spectrometer (LWS) in the mid- and far-infrared spectral region. In the mid-IR, along with its strong $O - H$ stretching mode (3.05 μm), water shows weaker bending and combination bands at 1666.67 cm^{-1} (6.00 μm) and 2222.22 cm^{-1} (4.50 μm), respectively, and the libration mode at 769.23 cm^{-1} (13.00 μm), which is usually blended with the grain silicate spectroscopic features along the line of sight to star forming regions in the ISM.[9]

After H_2, water is the second most abundant molecular species in the Universe and its gas-phase abundance in the ISM is even comparable to that of CO. Due to the high abundance of water in interstellar ices,[16] the amount of the other species is very often expressed in terms of the relative abundance with respect to H_2O, and thus considered as impurities. Among other solid species, CO, CO_2, CH_3OH, H_2CO, HCOOH, NH_3, CH_4, and OCS have been unambiguously identified,[9] while theoretical studies suggest that N_2 and O_2 might be trapped in the ice matrix as well.[17] It should be noted that although homonuclear molecules are IR inactive, they can become IR active when embedded in ice matrices. Interstellar ice

matrices are usually classified as (i) polar ices, if dominated by polar molecules like H_2O, CH_3OH, NH_3, OCS, H_2CO, HCOOH, and (ii) apolar ices, if they are dominated by molecules like CO, CO_2, CH_4, N_2, and O_2. Interstellar ices are believed to be a combination of both with a first polar (water-rich) layer and an apolar CO-dominated layer deposited on top of it during the catastrophic freeze-out of CO molecules in the cold core of molecular clouds.[18]

Infrared spectroscopy is a suitable technique for identifying interstellar species, particularly, in condensed phases. However, it requires that vibrations are IR active, condition which is fulfilled when the dipole moment changes during vibration. The IR spectrum of a water cluster is one of the primary tools to analyze the features of the aggregation processes in a water matrix[19–21]. Moreover, four vibrational modes of water, namely libration, bending, bulk stretching, and free-OH stretching, are essential to obtain relevant information about the water cluster itself in various astrophysical environments.[19–22]

However, there are some difficulties for the observation of interstellar ices in the mid-IR, such as the need for a background illuminating source being required for absorption, e.g. a protostar or a field star. Furthermore, peak positions, line widths, and intensities of molecular ice features need to be known and compared to laboratory spectra, which further depend on ice temperature, crystal structure of the ice, and mixing or layering with other species.[23–25] As a result, only a very limited number of species have been unambiguously detected in interstellar ices. CO is routinely observed from various ground-based facilities. In the solid phase, its abundance may vary from 3% to 20% of the water-ice. CO absorbance shows both polar and apolar band profiles. Soifer et al.[26] reported the detection of the fundamental vibrational band of CO at 4.61 μm (2169.20 cm^{-1}) in absorption toward W33A, based on the laboratory work of Mantz et al.[27]. The corresponding band profile consists of a broad (polar) component peaking at 2136.75 cm^{-1} (4.68 μm) and a narrow (non-polar) component peaking at 2141.33 cm^{-1} (4.67 μm).[28,29] CO_2 was detected in absorption at 657.89 cm^{-1} (15.20 μm) toward several IRAS sources by D'Hendecourt and Jourdain de Muizon[30], based on their laboratory work. The presence of CO_2 in ice mantles was found on

very few astrophysical objects before the launch of ISO,[16] which allowed to firmly establish the ubiquitous nature of CO_2.[31–33] In the ice phase, CH_3OH abundance varies between 5% and 30% with respect to H_2O. Its abundance can be even lower in some sources, such as Sgr A and Elias 16.[34] From ground-based observations, the stretching band of methanol at 2832.80 cm^{-1} (3.53 μm) was detected in massive protostars.[35–37] The first attempt of H_2CO observation was made by Schutte et al.[38], based on the absorption feature at 2881.84 cm^{-1} (3.47 μm), towards the protostellar source GL 2136 using the United Kingdom Infrared Telescope (UKIRT). They estimated the abundance of H_2CO to be $\sim$ 7% with respect to H_2O; however, only a small fraction of H_2O is mixed with H_2CO. Space-based ISO observations[39,40] estimated the formaldehyde abundance ranging between 1% and 3% in five high mass protostellar envelopes.[41] HCOOH was detected both in the solid and gas phase.[24,42,43] CH_4 was simultaneously detected in both gas and ice phases toward NGC 7538 IRS 9.[44] Infrared spectra from the Spitzer Space Telescope show a feature corresponding to the bending mode of solid CH_4 at 1298.70 cm^{-1} (7.7 μm);[45] in that work they derived its abundance to range from 2% to 8%, with the exception of some sources where abundances were found to be as high as $11 - 13\%$. Knacke et al.[46] claimed the first identification of NH_3 in interstellar grains from an IR absorption feature at 3367.00 cm^{-1} (2.97 μm) (NH stretching mode), a detection later proved to be wrong.[47] Eventually, the detection of NH_3 was reported by Lacy et al.[48], who assigned an absorption feature at 1109.88 cm^{-1} (9.01 μm) toward NGC 7538 IRS 9. Palumbo et al.[49] and Palumbo et al.[50], based on their laboratory work, identified toward a number of sources an absorption feature at 2040.82 cm^{-1} (4.90 μm) that can be assigned to OCS when mixed with CH_3OH.

Recently, the ROSINA mass spectrometer onboard the ESA's Rosetta spacecraft has discovered an abundant amount of molecular oxygen, O_2, in the coma of the 67P/Churyumov-Gerasimenko comet, thus deriving the ratio $O_2/H_2O = 3.80 \pm 0.85\%$.[51] Neutral mass spectrometer data obtained during the ESA's *Giotto* flyby are consistent with abundant amounts of O_2 in the coma of comet 1P/Halley, the O_2/H_2O ratio being evaluated to be $3.70 \pm 1.7\%$.[52]

This makes O_2 the third most abundant species. In the ISM, O_2 and N_2 are nearly absent in the gas phase because they are depleted on grains in the form of solid.[17] Since N_2 and O_2 do not possess dipole moment, they cannot be detected using radio observations. However, N_2 and O_2 might be detected by their weak IR active fundamental transition in solid phase, which lies around 4.3 μm for N_2 and around 6.4 μm for O_2.[23,53]

To date, infrared observations suggest that the ice mantles in molecular clouds are unambiguously composed of the few aforementioned molecules.[54] However, more complex species, such as complex organic molecules (COMs), are also expected to be frozen on ice grains in dense cores. The low sensitivity or low resolution of available observations combined with spectral confusion in the infrared region can cause the weak features due to solid COMs to be hidden by those due to more abundant ice species. The upcoming NASA's James Webb Space Telescope (JWST; `https://jwst.stsci.edu`) space mission set to explore the molecular nature of the Universe and the habitability of planetary systems promises to be a giant leap forward in our quest to understand the origin of molecules in space. The high-resolution of the spectrometers onboard the JWST will enable the search of new COMs in interstellar ices and will shed lights on different ice morphologies, thermal histories, and mixing environments. JWST will be able to map the sky and see right through and deep into massive clouds of gas and dust that are opaque in the visible. However, the large amount of spectral data provided by JWST could be analyzed only if extensive spectral laboratory and modeling datasets are available to interpret such data. The work presented here aims at gaining information on the effect of intermolecular interactions in interstellar relevant ices, thus providing some valuable new laboratory and computed absorption spectra of water-rich ices. These will be useful for the interpretation of future observations in the mid-infrared spectral region.

In this paper, a detailed systematic study of the four fundamental vibrational modes of water in presence of various molecular species with different concentration ratios has been carried out. Since water is the major component of interstellar ice matrix, the latter is

considered as composed of water molecules with the other compounds being impurities or pollutants. Since the hydrogen bonding network of pure water clusters in the solid state is strongly affected by increasing concentration of impurities, the spectra of the water pure ice is remarkably different from that of ice containing other species. Indeed, ice bands are very sensitive to intermolecular interactions,[55] with both strength and band profiles being affected.[20,21,56] The changes in the spectral behavior and band strengths are primarily due to molecular size, proton affinity, and polarity of the pollutants. To the best of our knowledge, there are not similar studies on liquid water systems as some of the impurity species chosen here are water-soluble. A large number of studies have been devoted to vibrational spectra of diluted aqueous solutions of species corresponding to the polar impurities we considered in the present study. However, the attention is usually focused on the variation of the vibrational properties of the solute and not of the solvent[57–59]. In a broader context, some infrared studies are available for the whole solubility range of some species[60,61].

This paper is organized as follows. In Section 2, we describe the methodology. In Section 3, we briefly discuss the experimental details. Results and discussions are presented in Section 4, and finally, in Section 5, the concluding remarks are reported.

2 Methodology

There are three established structures of water ice (with a local density of 0.94 g cm^{-3}) formed by vapor deposition at low-pressure. Two of them are crystalline (hexagonal and cubic) and one is a low-density amorphous form.[62] High-density amorphous water ice (with a local density 1.07 g cm^{-3}) also exists and can be formed by the vapor deposition at low temperatures.[62] Pradzynski et al.[63] experimentally analyzed the number of water molecules needed to generate the smallest ice crystal. According to that study, the appearance of crystallization is first observed for 275 ± 25 and 475 ± 25 water molecules, these aggregates showing the well-known band of crystalline ice around 3200 cm^{-1} (in the OH-stretching

region). Blake and Jenniskens[62] found experimentally that the onset of crystallization occurs at 148 K. Since we aim to validate our calculations for the low-temperature and low-pressure regime, we focus on the amorphous ices showing a peak in the IR spectrum at around 3400 cm^{-1}. However, since it is not clear how many water molecules are necessary to mimic the amorphous nature of water ice, we considered pure water clusters of different sizes and studied their absorption spectra. For this purpose, we have optimized water clusters of increasing size at different levels of theory. The water clusters considered are: $2H_2O$ (dimer), $4H_2O$ (tetramer), $6H_2O$ (hexamer), $8H_2O$ (octamer), and $20H_2O$, with their structures being optimized with three different methods (B3LYP, B2PLYP, and QM/MM) as explained in Section 2.1. The specific choice of these cluster models is based on experimental outcomes. Experimentally, it has been demonstrated that the water dimer has a nearly linear hydrogen bonded structure.[64] The water clusters with 4 H_2O molecules are cyclic in the gas phase.[65] Moving to a 6 H_2O cluster, different structures are available: a three-dimensional cage in the gas phase[66] and cyclic (chair) in the liquid helium droplet.[67] For $8H_2O$, an octamer cube has been found in gaseous states.[19] Finally, the $20H_2O$ cluster has been considered to check the direct effect of the environment, with more details being provided in the computational detail section.

Using the optimized structures of the series of clusters above, harmonic frequencies have been computed and the band strengths of the four fundamental modes have been calculated by assuming the integration bounds as shown in Table 1. Similar integration bounds (except for free-OH stretching mode) were considered in Bouwman et al.[20] and Öberg et al.[21]. Similar absorption profiles of four fundamental modes of pure water have been obtained from our calculations, with their intensity, band positions and strengths varying for the different cluster sizes and levels of theory used. It is thus essential to find the best compromise between accuracy and computational cost. This means to understand which is the smallest cluster and the cheapest level of theory able to provide a reliable description of water ice. To this aim, we have compared the band positions and the corresponding band strengths of

the four vibrational fundamental modes of water obtained with different cluster sizes and different methodologies, to experimental work.

Table 1: Integration bounds for the four fundamental modes of vibration.

Species	Assignment	Integration bounds	
		Lower (cm^{-1})	Upper (cm^{-1})
H_2O	$\nu_{libration}$	500	1100
	$\nu_{bending}$	1100	1900
	$\nu_{bulk-stretching}$	3000	3600
	$\nu_{free-OH-stretching}$	3600	4000

While the outcome of this comparison will be discussed later in the text, here we anticipate that the $4H_2O$ cluster in the c-tetramer configuration will be chosen as water ice unit. To investigate the effect of impurities, a number of impurity molecules have been added in order to obtain the desired ratio, as shown in Table 2. For example, in order to get 2:1 ratio of water:impurity(x), we considered 4 water molecules hooked up with 2 'x' molecules. However, for some systems, to have more realistic features of the water cluster, we needed to consider more water molecules. Since it is known that the water ice clusters containing six H_2O molecules are the form of all natural snow and ice on Earth[68], we also present a case with six H_2O molecules together as a unit (see Figure S1 in the Supporting Information, SI). The cyclic hexamer (chair) configuration of the water cluster containing six H_2O has been found the most stable,[19] and considered in our calculations.

Table 2: Ice mixture composition details.

H_2O:X	**Total no. of molecules**	**No. of water molecules**	**No. of pollutant molecules**
1:0.25	5	4 (80.0%)	1 (20.0%)
1:0.50	6	4 (66.7%)	2 (33.3%)
1:0.75	7	4 (57.1%)	3 (42.9%)
1:1.00	8	4 (50.0%)	4 (50.0%)

Notes. Contributions in percentage are provided in the parentheses.

In Figure 1a, we present the optimized water clusters for the c-tetramer configuration. The same structure was considered by Ohno et al.[19] and others[69–71]. Since four H atoms are available for interacting with the impurities by means of hydrogen bond, in our calculations we can reach up to a 1 : 1 ratio between the water and the impurity (i.e., we can reach up

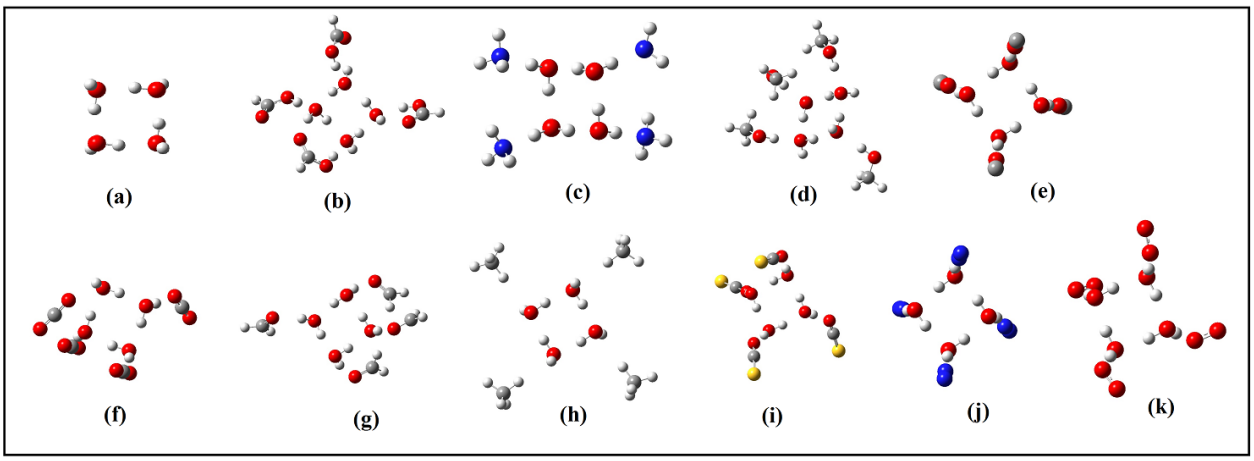

Figure 1: Optimized structures for (a) pure water and for the 4 : 4 concentration ratio: (b) $H_2O - HCOOH$, (c) $H_2O - NH_3$, (d) $H_2O - CH_3OH$, (e) $H_2O - CO$, (f) $H_2O - CO_2$, (g) $H_2O - H_2CO$, (h) $H_2O - CH_4$, (i) $H_2O - OCS$, (j) $H_2O - N_2$, (k) $H_2O - O_2$ clusters.

to 50% concentration of the impurity in the ice mixture).

In order to understand the effect of impurities on the band strengths of the four fundamental bands considered, we have calculated the area under the curve for each band for different mixtures of pure water and pollutants. The band strength has then been derived using the following relation (introduced in Bouwman et al.[20] and Öberg et al.[21]):

$$A^{band}_{H_2O:x=1:y} = \int_{band} I_{H_2O:x=1:y} \times \frac{A^{H_2O}_{band}}{\int_{band} I_{H_2O}}, \tag{1}$$

where $A^{band}_{H_2O:x}$ is the calculated band strength of the vibrational water mode in the $1 : y$ mixture, $I_{H_2O:x=1:y}$ is its integrated area, $A^{H_2O}_{band}$ is the band strength of the water modes available from the literature, and $\int_{band} I_{H_2O}$ is the integrated area under the vibrational mode for pure water ice. The experimental absorption band strengths of the three modes of pure water ice are taken from Gerakines et al.[22], who carried out measurements with amorphous water at 14 K. The adopted values are 2×10^{-16}, 1.2×10^{-17}, 3.1×10^{-17} cm molecule^{-1}, for the bulk stretching (3280 cm^{-1}), bending (1660 cm^{-1}), and libration mode (760 cm^{-1}), respectively. Our *ab-initio* calculations refer to the temperature at 0 K. For the calculation of the band strengths, we are considering the strongest feature of that band. Since for the

free-OH stretching mode no experimental values exist, we consider the result $A^{H_2O}_{free-OH} = 2.09 \times 10^{-17}$ and 2.52×10^{-17} cm molecule^{-1} for the c-tetramer and hexamer water clusters, respectively.

2.1 Computational details

As already mentioned, quantum-chemical calculations have been performed to evaluate the changes of the absorption features of four different fundamental modes, namely, (i) libration, (ii) bending, (iii) bulk stretching, and (iv) free-OH stretching of water in the presence of impurities (CO, CO_2, CH_3OH, H_2CO, HCOOH, CH_4, NH_3, OCS, N_2, and O_2). High-level quantum chemical calculations (such as CCSD(T) method and hybrid force field method) are proven to be the best suited for reproducing the experimental data.[72,73] However, due to the dimension of our targeted species, these levels of theory are hardly applicable.

As already anticipated, different DFT functionals have been tested. Most computations have been carried out using the B3LYP hybrid functional[74,75] in conjunction with the 6-31G(d) basis set (Gaussian 09 package[76]). Some test computations have also been performed by using the B2PLYP double-hybrid functional[77] in conjunction with the the m-aug-cc-pVTZ basis set,[78] in which the *d* functions have been removed on hydrogen atoms (maug-cc-pVTZ-*d*H). In this case, harmonic force fields have been obtained employing analytic first and second derivatives[79] available in the Gaussian 16 suite of programs.[80] The reliability and effectiveness of this computational model in the evaluation of vibrational frequencies and intensities have been documented in several studies (see, for example, ref. 81). We have also performed anharmonic calculations (at the B3LYP/6-31G(d) level) for the H_2O-CO and H_2O-NH_3 systems in order to check the effect of anharmonicity on the band strength profiles of the four water fundamental modes.

The spectral features of the astrophysical ices can be altered in both active (direct) and passive (bulk) ways. Following a consolidated practice,[82] to include the passive contribution of the bulk ice on the spectral properties of the ice mixtures considered, we embedded our

explicit cluster in a continuum solvation field to represent local effects on the ice mixture. To this end, we resorted to the integral equation formalism (IEF) variant of the Polarizable Continuum Model (PCM).[83] The solute cavity has been built by using a set of interlocking spheres centered on the atoms with the following radii (in Å): 1.443 for hydrogen, 1.925 for carbon, 1.830 for nitrogen, and 1.750 for oxygen, each of them scaled by a factor of 1.1, which is the default value in Gaussian. For the ice dielectric constant, that of bulk water ($\varepsilon = 78.355$) has been used, although any dielectric constant larger than about 30 would lead to very similar results. In addition, we have also performed QM/MM geometry optimizations of a pure water cluster containing 4 H_2O molecules, in which all but one molecule at the square vertexes were put in the MM layer (see Figure 2, left panel). A pure water cluster system containing 20 H_2O molecules has also been considered. For this, we started from the coordinates of the full QM optimization and selected two alternative sets of four innermost molecules at the center of the cluster with a complete hydrogen bond network (determined with a geometric criterion[84]) with first neighbor water molecules; the remaining 16 molecules were described at the MM level (see Figure 2, right panel). All QM/MM[85] calculations were carried out with the Gaussian 16[80] code (rev. C01) using the hybrid B3LYP functional in conjunction with the 6-31 G(d) basis set. Atom types and force field parameters for water molecules in the MM layer were assigned according to the SPC-Fw flexible water model;[86] the choice was driven by (i) the necessity for a flexible, 3-body classical water model and (ii) the accuracy with which the selected model reproduced ice I_h properties. Solvent effects were mimicked by using PCM.[87] The vibrational analysis results from QM/MM calculations are provided in Tables S10, S11, and S12.

3 Experimental Methods

Literature laboratory data are here used whenever possible to constrain simulations.[20,21] In the cases of formic acid, ammonia, and methanol in water ice, new experiments have been

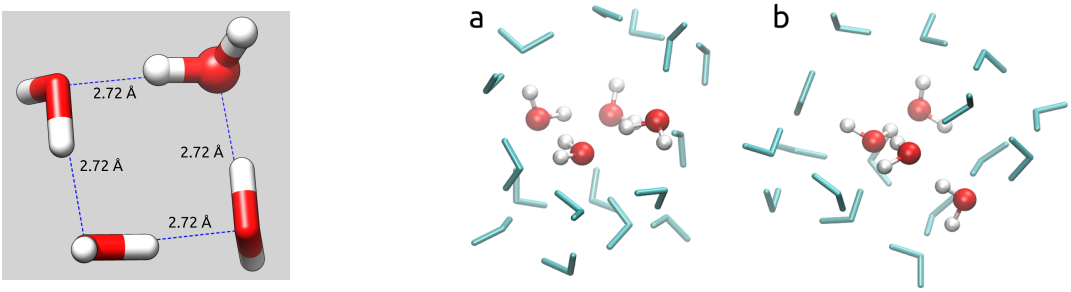

Figure 2: **Left:** 4 water system; the single QM water molecule is depicted in ball and stick representation and the 3 MM molecules in licorice representation; O-H distances are indicated too. It is to be noted that the four H_2O can be considered equivalent, **Right:** Innermost water molecules described at QM level (ball and stick) and surrounding molecules described at MM level (lines) for the $20H_2O$ system. (a) Configuration 1. (b) Configuration 2.

performed using the high vacuum (HV) Portable Astrochemistry Chamber (PAC) at the Open University (OU) in the United Kingdom. A detailed description of the system is reported elsewhere.[88] Briefly, the main chamber is a commercial conflat flange cube (Kimball Physics Inc.) connected to a turbo molecular pump (300 l/s), a custom made stainless steel dosing line through an all metal leak valve, a cold finger of a closed-cycle He cryostat (Sumitomo Cryogenics) and two ZnSe windows suitable for IR spectroscopy. During operation, the base pressure in the chamber is in the 10^{-9} mbar range, and the base temperature of the cold finger is 20 K. In thermal contact with the cryostat, the substrate is a ZnSe window (20 mm x 2 mm). A DT-670 silicon diode temperature sensor (LakeShore Cryotronics) is connected to the substrate to measure its temperature, while a Kapton flexible heater (Omegalux) is used to change its temperature. Diode and heater are both connected to an external temperature controller (Oxford Instruments).

Gaseous samples were prepared and mixed in a pre-chamber (dosing line) before being dosed into the main chamber through an all metal leak valve. A mass-independent pressure transducer was used to control the amount of gas components mixed in the pre-chamber. Chemicals were purchased at Sigma-Aldrich with the highest purity available [HCOOH (>95%), NH_3 (99.95%), and CH_3OH (99.8%)]. Ices were grown *insitu* by direct vapour deposition onto the substrate at normal incidence via a 3 mm nozzle that is 20 mm

away from the sample. Infrared spectroscopy was performed in transmission using a Fourier Transform infrared (FTIR; Nicolet Nexus 670) spectrometer with an external Mercury cadmium telluride (MCT) detector. A background spectrum comprising 512 co-added scans was acquired before deposition at 20 K and used as reference spectrum for all the spectra collected after deposition to remove all the infrared signatures along the beam pathway that were not originated by the ice sample. Each IR spectrum is a collection of 256 co-added scans. The IR path was purged with dry compressed air to remove water vapour.

4 Results and Discussions

In this section, first of all, the pure water ice will be addressed in order to establish the best compromise between accuracy and computational cost for the description of the water ice unit cell. To this aim, we will resort on the comparison with experiment. Then, we will move to the ice containing impurities. To further proceed with the validation of our protocol, water ice containing HCOOH, NH_3, CH_3OH, CO, and CO_2 as impurities will be investigated, thus exploiting the comparison between experiment and computations. This will also involve, as mentioned above, new measurements. Finally, in the last part, our protocol will be extend to the study of water ices with H_2CO, CH_4, N_2, and O_2 as impurities.

4.1 Part 1. Validation

4.1.1 Band strength of pure water

In Table 3, the water band positions obtained with different methods and different sizes of the water cluster are compared with experimental data. Since computations provide several frequencies corresponding to a single mode of vibration, for the sake of comparison, we have reported the computed frequencies of the four fundamental modes after convolving them with a Gaussian function with an adequate width[89] (all transition frequencies are collected in the Appendix, Table 5). The comparison of Table 3 is graphically summarized in Figure

3. The left panel shows the average deviation of the band position of three fundamental modes of water (libration, bending, and stretching) from the experimental counterpart [22]. It is interesting to note that the band positions obtained using the tetramer configuration and the B3LYP/6-31G(d) level of theory provides the best agreement. The right panel shows the average deviation of the band strengths from experiments. QM/MM calculations for the 20 water-molecule cluster (as described in the computational details) show the minimum deviation from experimental data. The results obtained for the tetramer configuration, both at the B3LYP and B2PLYP level, also provide small deviations. Based on the results of the comparison carried out, the B3LYP/6-31G(d) level of theory and the tetramer configuration have been found to be a suitable combination to describe the water cluster with a limited computational cost.

Table 3: Absorption band strengths and band positions (within parentheses; in cm^{-1}) of pure water ice.

Vibration mode	Experiment Gerakines et al. [22]	Computed values in cm molecule^{-1} and band position in cm^{-1}			
		Dimer	c-Tetramer	c-Hexamar (chair)	Octamer (cube)
		B3LYP-631G(d)	B3LYP-631G(d)	B3LYP-631G(d)	B3LYP-631G(d)
Libration	3.1×10^{-17} (760)	2.70×10^{-17}(670)	2.40×10^{-17}(733)	1.17×10^{-16}(870)	1.27×10^{-17}(848)
Bending	1.2×10^{-17} (1660)	2.23×10^{-17}(1710)	4.18×10^{-17}(1714)	4.62×10^{-17}(1730)	6.85×10^{-17}(1717)
Stretching	2.0×10^{-16} (3280)	8.27×10^{-17}(3540)	3.11×10^{-16}(3298)	5.53×10^{-16}(3220)	3.89×10^{-16}(3320)
Free-OH	–	1.35×10^{-17}(3810)	2.10×10^{-17}(3775)	2.52×10^{-17}(3780)	1.52×10^{-17}(3787.81)
Vibration mode	Experiment Gerakines et al. [22]	Computed values in cm molecule^{-1} and band position in cm^{-1}			
		c-Tetramer	$1H_2O$(QM)+$3H_2O$(MM)	$4H_2O$(QM)+$16H_2O$(MM)	
		B2PLYP/m-aug-cc-pVTZ	B3LYP-631G(d)	B3LYP-631G(d)	
Libration	3.1×10^{-17} (760)	3.94×10^{-17}(714)	7.91×10^{-17}(669)	4.9×10^{-17}(720)	
Bending	1.2×10^{-17} (1660)	2.93×10^{-17}(1635)	2.37×10^{-17}(1431)	1.88×10^{-17}(1426)	
Stretching	2.0×10^{-16} (3280)	2.97×10^{-16}(3477)	2.68×10^{-17}(3593)	1.76×10^{-16}(3565)	
Free-OH	–	2.40×10^{-17}(3865)	6.24×10^{-18}(3797)	2.52×10^{-17}(3636)	

In the following sections, the results for water ice with HCOOH and NH_3 as impurities are first reported and discussed, thereby exploiting the outcomes of new experiments. Then, we move to the CH_3OH-H_2O ice for which new experimental results have been obtained. For the last two cases addressed, namely CO-H_2O and CO_2-H_2O, the experimental data for

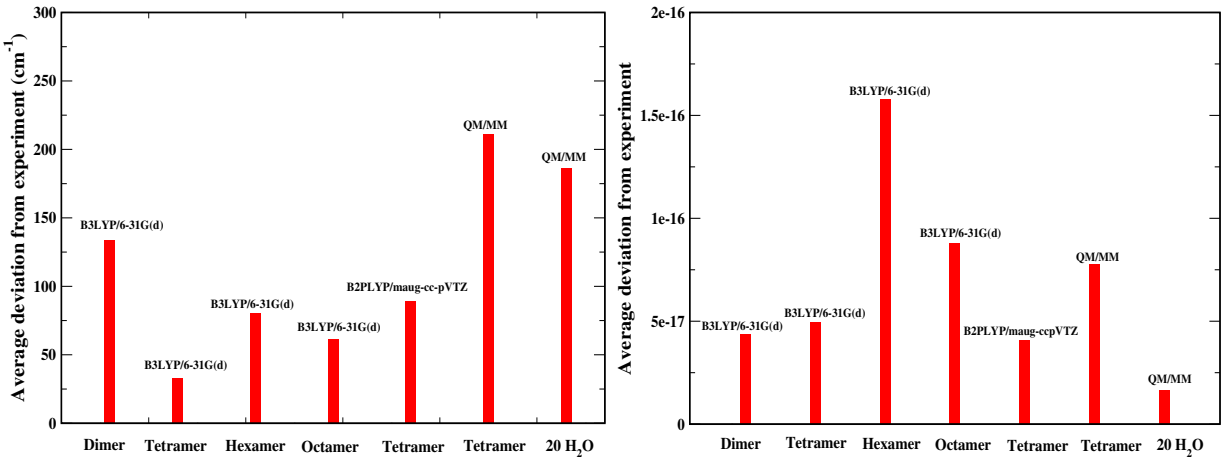

Figure 3: Deviation of computed band positions (left panel) and band strengths (right panel) from experiments.

the comparison have been taken from the literature. Unless otherwise stated, we use the c-tetramer configuration for the rest of our calculations.

4.1.2 HCOOH ice

Infrared spectra were measured for various mixtures of H_2O and HCOOH ice deposited at 20 K, as explained in the experimental details section (see Section 3). These, normalized with respect to the O-H stretch, are shown in Figure 4a. A minor contamination due to CO_2 was detected in some experiments. In all experiments, the amount of CO_2 deposited in the ice was found to be between 1000 and more than 100 times less abundant than H_2O and HCOOH, respectively. Therefore, we do not expect that the CO_2 contamination affects the recorded IR spectra profiles.

The mixture ratios were determined from the fit of the the spectrum of a selected mixture, the measurement of the area of the water band at 3333.33 cm^{-1} (3.00 μm), and the comparison with the pure water counterparts. For HCOOH, the absorption area is measured at 1700 cm^{-1}. In fact, HCOOH has the strongest mode at 1694.92 cm^{-1} (5.90 μm) which corresponds to its C=O stretching mode. But the feature overlaps with the position of the OH bending mode of solid water at 1666.67 cm^{-1} (6.00 μm). The contribution from the water bending mode at $\sim$1700 cm^{-1} has been subtracted from the total area before the band

strength mentioned above being used to calculate the amount of HCOOH in the ice mixture. The band strengths used here are 2.0×10^{-16} for H_2O[22] and 6.7×10^{-17} for HCOOH.[24,90] Another relatively weaker mode of HCOOH at 1388.89 cm^{-1} (7.20 μm) was also considered because the corresponding region is free from interfering transitions.[24] As seen in Figure 4a, the HCOOH:H_2O ratios cover the 0.05 to 3.46 range. In this respect, it is worthwhile noting that the abundances of solid phase HCOOH in the interstellar ices vary between 1% to 5% with respect to the H_2O ice.[91]

Moving to the computational study, Figure 1b shows how the HCOOH molecules are bonded to the water molecules to form the 4 : 4 H_2O-HCOOH mixture used in our calculations. In the Appendix, the absorption band profiles of the H_2O-HCOOH clusters with different impurity concentrations are shown (see Figure 14). The transition frequencies and the corresponding strongest intensity values, obtained at the B3LYP/6-31G(d) level, are given in the Appendix (see Table 6). Calculations have also been carried out using the B2PLYP functional, the results being summarized in Tables S1, S2, S3, S4, and S5 in the SI.

To investigate how the band strength varies with impurity concentrations, the data are fitted with a linear function $A_{eff} = a \cdot [X] + b$, where X = HCOOH, NH_3, CH_3OH, CO, CO_2, H_2CO, CH_4, OCS, N_2, and O_2. The coefficient 'a' provides the information whether the band strength increases or decreases by increasing the concentration of X, [X], and the coefficient 'b' indicates the band strength of the vibration mode in the absence of impurities. The fitting coefficients, for all impurity considered, are provided in Table 4. In Figure 5a, the band strength profile as a function of the concentration of HCOOH is shown.

4.1.3 NH_3 ice

Most of the intense modes of ammonia overlap with the dominant features due to water and silicates. However, when ammonia is mixed with H_2O ice, it forms hydrates that show an intense mode at 2881.84 cm^{-1} (3.47 μm),[16] which lies in a relative clear region. Another

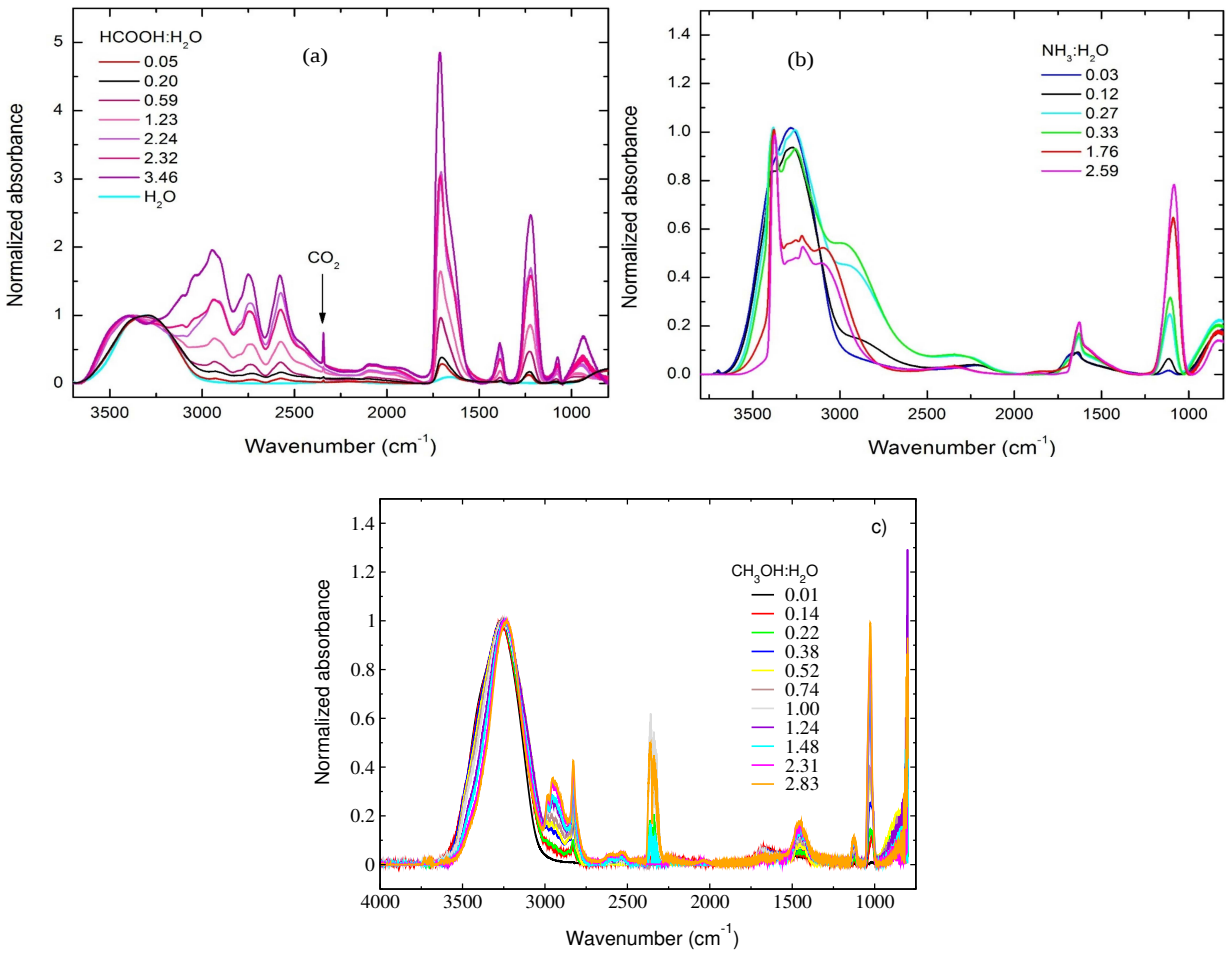

Figure 4: (a) IR spectra for different HCOOH:H_2O ice mixtures deposited at T= 20 K. (b) IR spectra for different NH_3:H_2O ice mixtures deposited at T= 20 K. (c) IR spectra of different CH_3OH:H_2O ice mixtures deposited at T= 30 K. The color legend is explained in the insets. All IR spectra are normalized with respect to the O-H stretching band.

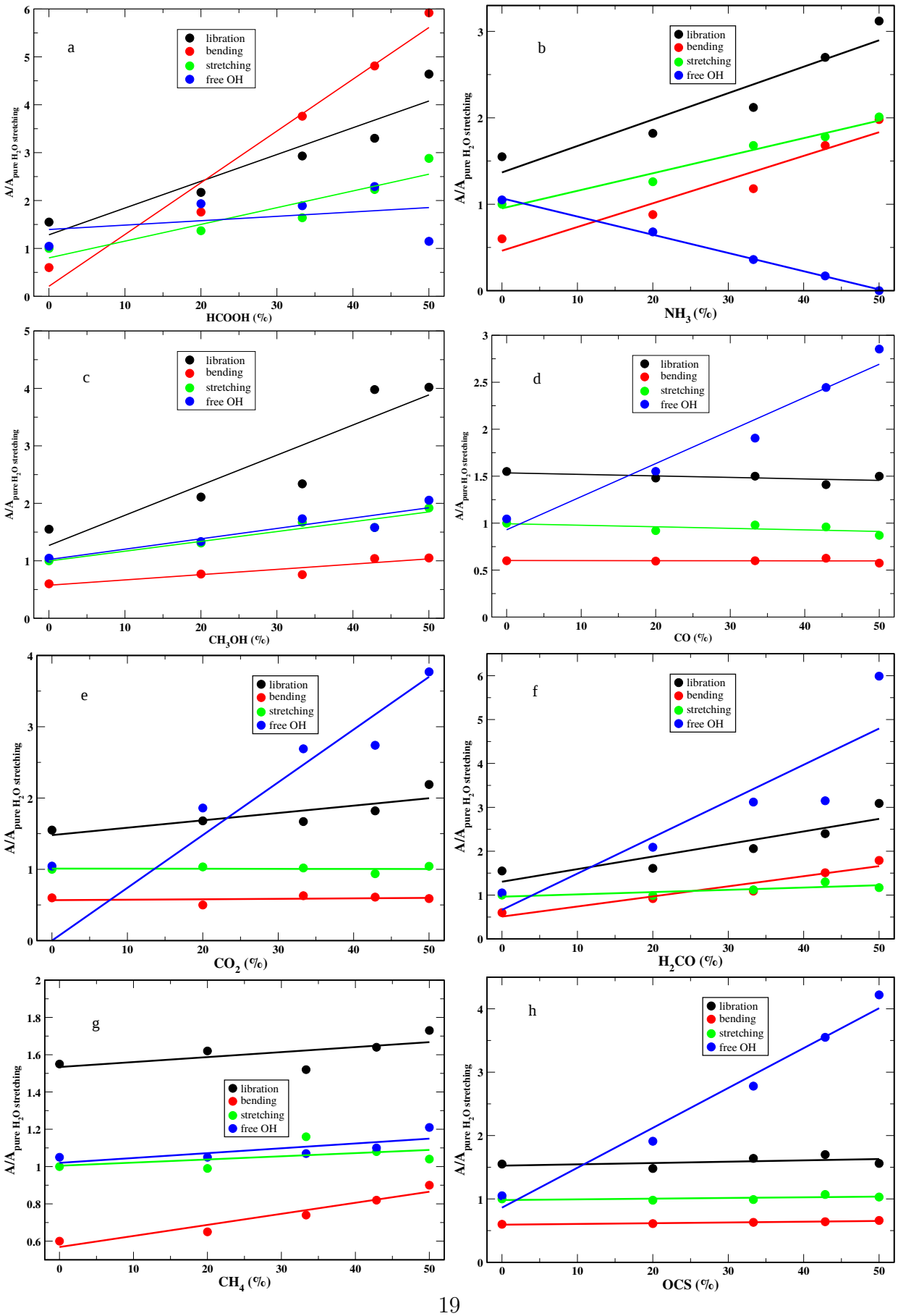
a
b
c
d
e
f
g
h
libration
bending
stretching
free OH
A/A pure H2O stretching
HCOOH (%)
NH3 (%)
CH3OH (%)
CO (%)
CO2 (%)
H2CO (%)
CH4 (%)
OCS (%)

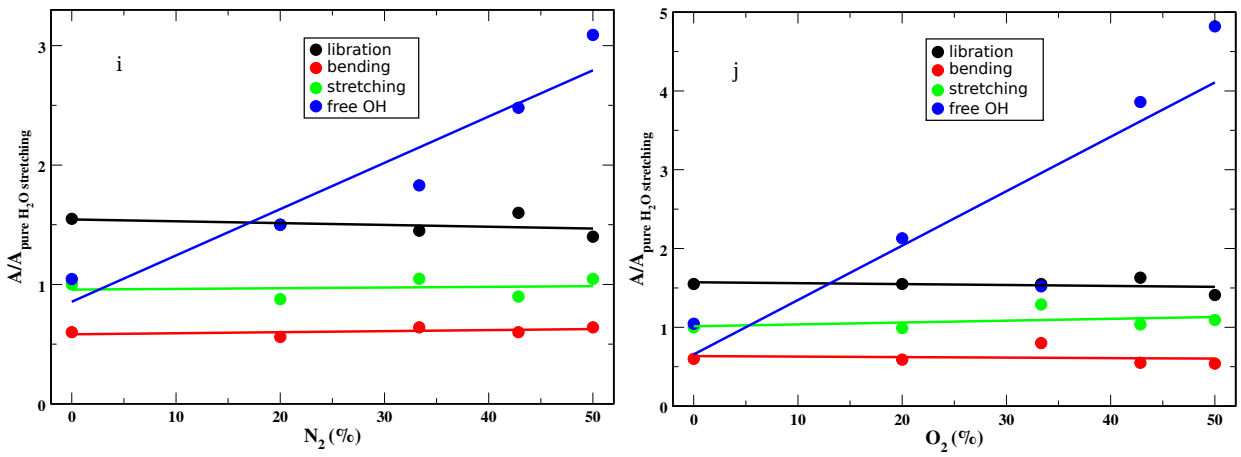

Figure 5: Band strengths of the four fundamental vibration modes of water for (a) $H_2O - HCOOH$, (b) $H_2O - NH_3$, (c) $H_2O - CH_3OH$, (d) $H_2O - CO$, (e) $H_2O - CO_2$, (f) $H_2O - H_2CO$, (g) $H_2O - CH_4$, (h) $H_2O - OCS$, (i) $H_2O - N_2$, and (j) $H_2O - O_2$ clusters with various concentrations. The water c-tetramer configuration was used for pure water.

characteristic feature of ammonia is the umbrella mode at 1111.11 cm^{-1} (9.00 μm), which is relatively intense, but it often overlaps with the CH_3 rocking mode of methanol, thus leading to an overestimation of the abundance of ammonia.

In this work, infrared spectra were recorded for various mixing ratios of H_2O-NH_3 ice deposited at 20 K. The IR spectra, normalized with respect to the most intense bend (i.e. the O-H stretching mode), are shown in Figure 4b. Mixing ratios were derived by measuring the areas of the selected bands for H_2O band (at 2220 cm^{-1})[92] and for NH_3 (umbrella mode band at 1070 cm^{-1}),[93] with a procedure analogous to that introduced in the previous section for HCOOH.

Figure 1c shows the optimized geometry of the H_2O-NH_3 system with a 4 : 4 ratio as obtained from our quantum-chemical calculations. In the Appendix, Figure 15 depicts the absorption band profiles of H_2O-NH_3 mixtures with various concentrations. The transition frequencies and the corresponding intensity values are provided in the Appendix as well (see Table 6). The vibrational analysis has also been carried out at a higher level of theory, thereby using the B2PLYP functional. The results are reported in Tables S6, S7, S8, and S9 in the SI. Figure 5b shows the band strengths as a function of the concentration of the

impurity under consideration, i.e. NH_3.

4.1.4 Comparison between experiment and simulations

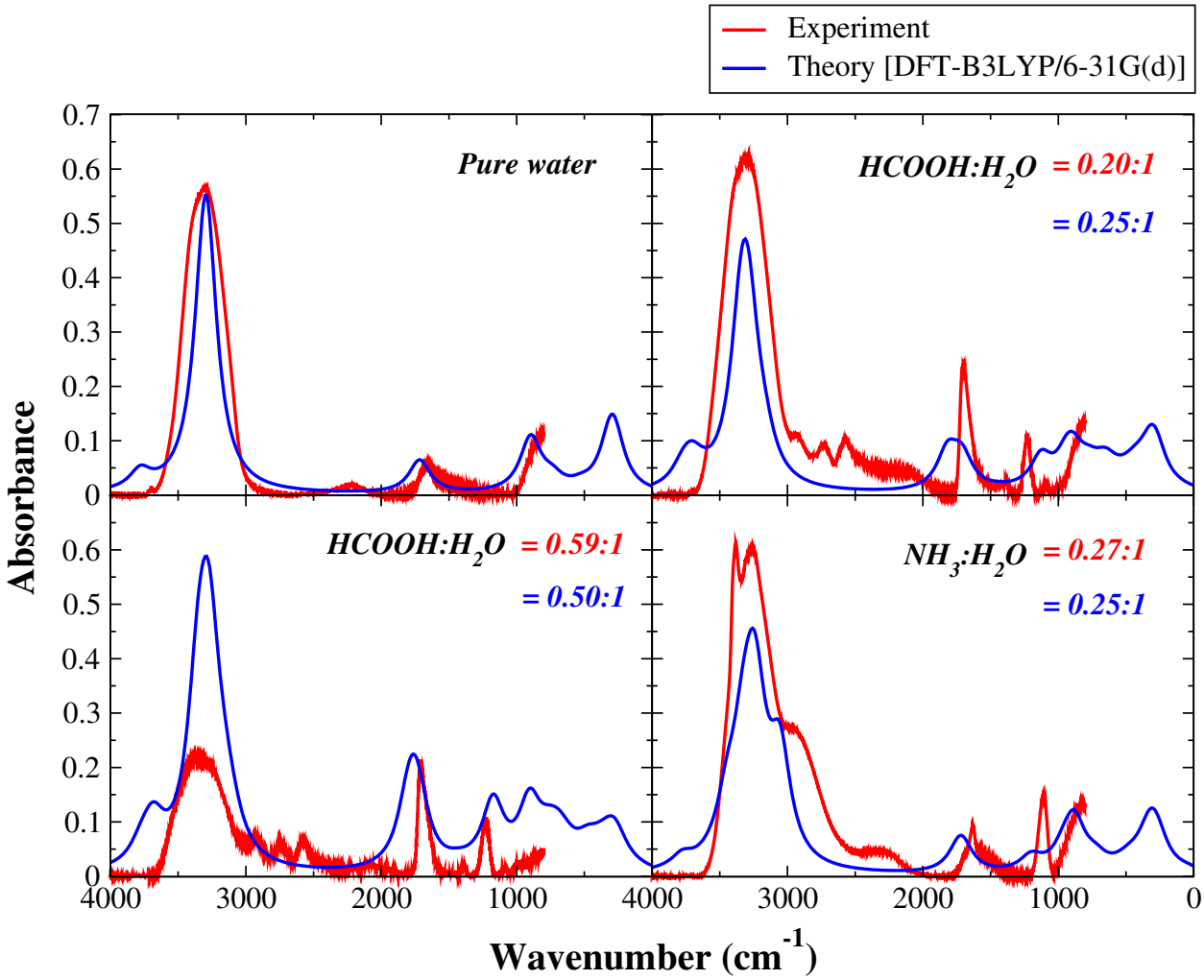

Figure 6: Comparison of computed and experimental IR spectra (0 - 4000 cm^{-1}) for pure water as well as water with HCOOH and NH_3 as impurities. We have used harmonic frequencies for the computed spectra and the intensity is scaled with a factor 1000 to have best match with the experimental one.

In Figure 6, the comparison between experimentally obtained spectra and our computed spectra for pure water, H_2O-HCOOH mixture, and H_2CO-NH_3 mixture is shown. We note a good agreement between experimental and theoretical absorption spectra. Figure 7 shows the comparison between the experimental (dotted lines) and theoretical (solid and dashed lines) band strengths of the four water bands as a function of the concentration of HCOOH and

NH_3. From Figure 7, it is evident that the experimental strength of the libration and bending modes increases by increasing the concentration of HCOOH. On the contrary, the strength of the stretching and free OH modes shows a decreasing trend. These behaviors should be compared with the B2PLYP/mug-cc-pVTZ (dashed) and B3PLYP/6-31G(d) (solid) trends. For the libration and bending band strength profiles, there is a qualitative agreement with experiments. In the case of the stretching and free OH modes, theoretical band strength profiles deviate from experimental work. The lack of experimental data in the 3600-4000 cm^{-1} range (see Figure 4a) may have contributed to this disagreement. Concerning the comparison of the two levels of theory, it is noted that there is a rather good agreement. In case of H_2O-HCOOH mixture, HCOOH can act as both hydrogen bond donor and hydrogen bond acceptor. We considered both the interactions and noted that, if we consider HCOOH as H-bond acceptor, the band strength of three modes (libration, bending, and stretching) are lower with respect to case where HCOOH was treated as H-bond donor. But in the case of the free-OH mode, the band strength slope increases (See Figure 12 in the Appendix).

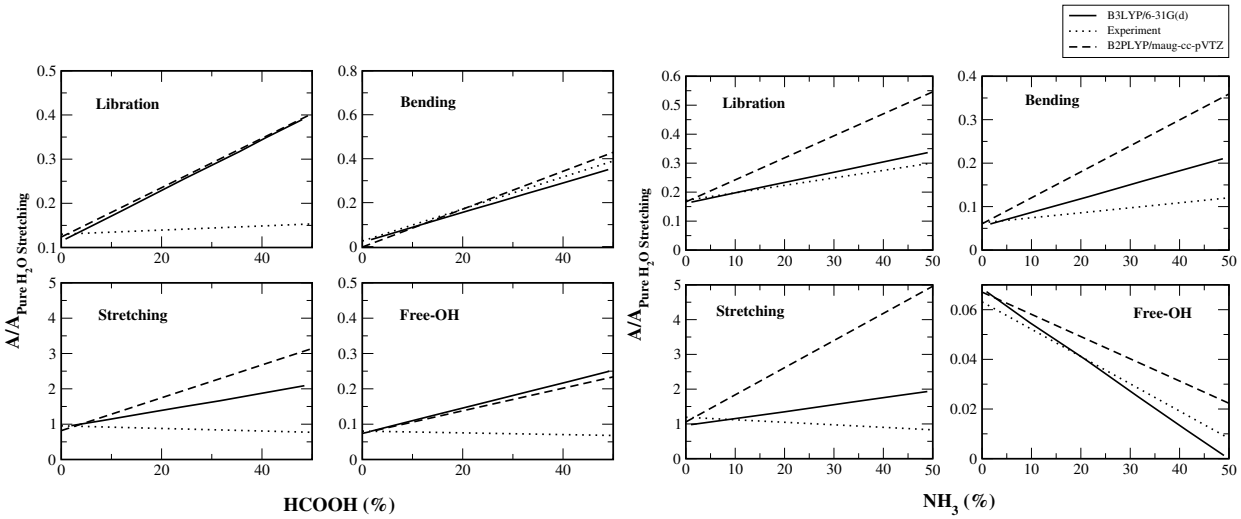

Figure 7: Comparison between the calculated and experimental band strength profiles with various concentration of HCOOH and NH_3.

Moving to ammonia, the experimental data of Figure 7 show that the band strength of the free-OH stretching mode nearly vanishes when a 50% concentration of the impurity (NH_3) is reached. This feature interestingly supports our calculated spectra shown in the

Appendix (see Figure 15 last panel). Libration and bending modes have, instead, an opposite trend, with the band strength increasing by increasing the concentration of NH_3. The band strength of the stretching mode shows a slightly decreasing trend with the concentration of NH_3. From the inspection of Figure 7 it is evident that both sets of theoretical results (B3LYP and B2PLYP) are in reasonably good agreement with experimental data for the libration, bending, and free-OH modes. Interestingly, the results obtained using the lower level of theory are in better agreement with experiments. In Figure 11 (in the Appendix), the comparison of band strengths evaluated using (a) harmonic and (b) anharmonic calculations is shown. To investigate the effect of anharmonicity on the band strengths, we have only considered fundamental bands in the 0 to 3600 cm^{-1} frequency range. From our experimental study on the H_2O-NH_3 system, as already mentioned, we obtained an increasing trend of the band strength for the libration, bending, and stretching modes with the increase in concentration of NH_3, whereas the band strength decreases for the free OH mode and tends to zero with 50% concentration of NH_3. When using harmonic calculations for all four fundamental modes, trends similar to what obtained from experiment were found. But, if we consider anharmonic calculations, only the behavior of the stretching mode is well reproduced. All other modes deviate from the experimental results. While not claiming that harmonic calculations are better than the anharmonic ones, this comparison seems to suggest that the former show a better error compensation. A similar outcome has been obtained for the H_2O-CO system and will be briefly addressed later in the text.

Based on the comparisons discussed above, the B3LYP/6-31G(d) level of theory provides reliable results. Therefore, it has been employed in the following investigations. First of all, the comparison between computed and experimental band strengths for the H_2O-CH_3OH, CO-H_2O, and CO_2-H_2O mixtures will be considered to further support its suitability.

4.1.5 CH_3OH ice

In this work, the effect of the CH_3OH concentration on the band profiles of water ice has been experimentally investigated. In the case of methanol, CO_2 gas is still present in the system (i.e., outside the vacuum chamber) in quantities that vary in time causing negative and/or positive contributions to CO_2 gas-phase absorption features with respect to the background spectrum, as evident in Figure 4c at $\sim$2340 cm^{-1}. Such contamination is most likely due to the dosing line, but its negligible amount should not affect the final results. Figure 4c shows the experimental absorption spectra for various CH_3OH-H_2O ice mixtures deposited at T= 30 K. The spectra are normalized to 1 with respect to the maximum of the O-H stretch band.

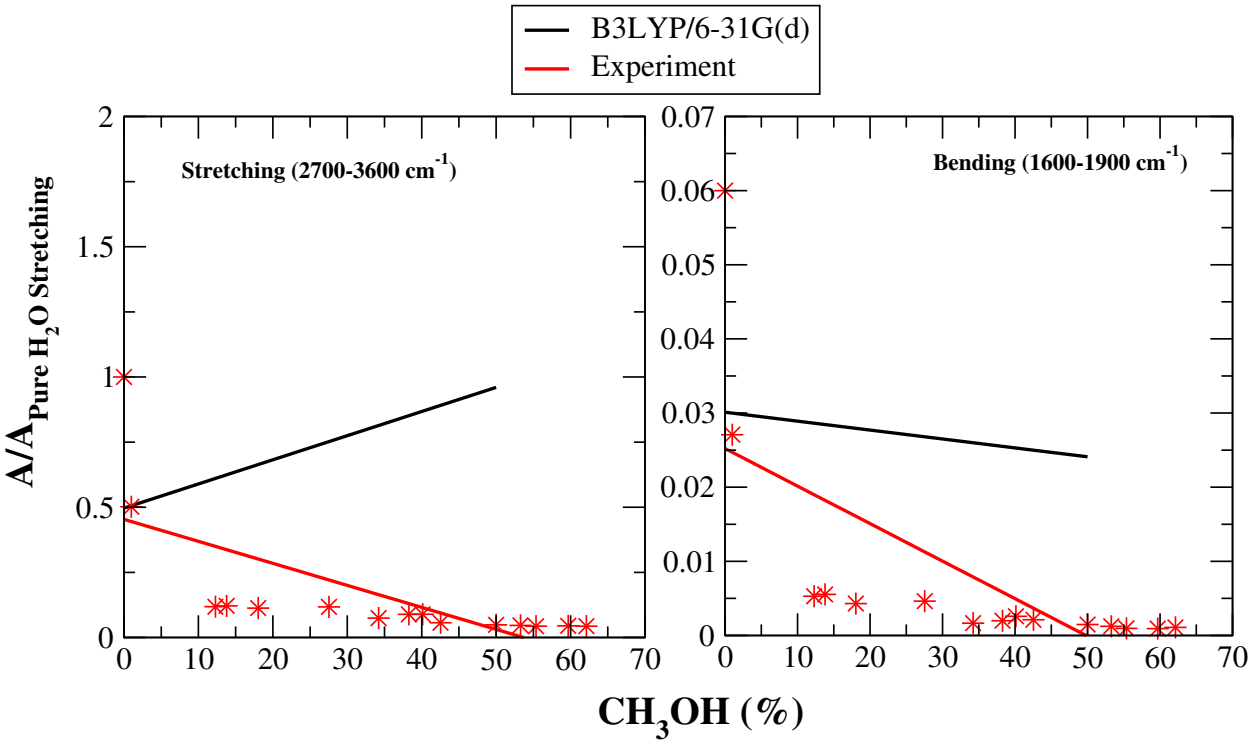

Figure 8: Comparison between calculated and experimental band strength profiles as a function of CH_3OH concentration. Stars represent the experimental data points.

Figure 1d shows the optimized structure of the H_2O-CH_3OH mixture with a 4 : 4 concentration ratio. It is noted that a weak hydrogen bond is expected to be formed. The simulated IR spectra for different concentrations are shown in Figure 16 (in the Appendix). Peak

positions, integral absorption coefficients, and band assignments for various H_2O-CH_3OH mixtures are collected in Table 6 in the Appendix. The computed band strengths as a function of different concentrations are shown in Figure 5c. The computed strength of the bending mode gradually increases with CH_3OH concentration (see Figure 8; right panel), which is in qualitative agreement with the experimental results.[88] In case of the stretching mode, computationally, a slight increasing trend of the band strength is noted, whereas experimental results show an opposite trend (see Figure 8; left panel). Because of the lack of experimental spectra, we cannot compare the band strength of the libration and free OH modes. In case of H_2O-CH_3OH mixtures, methanol can act as both hydrogen bond donor and hydrogen bond acceptor. We considered both possibilities and found that if we consider methanol as hydrogen bond donor, the band strength of all four modes show an increasing trend. On the other hand, if we consider methanol as hydrogen bond acceptor, the band strengths of three modes, namely libration, bending, and stretching, present trends similar to the previous case (where methanol acts as hydrogen bond donor), while the free-OH band shows a less pronounced behavior (see Figure 13 in the Appendix).

4.1.6 CO ice

Figure 1e depicts the H_2O-CO optimized structure with a 4 : 4 concentration ratio: the four CO molecules interact with the H atoms of the water molecules not involved in the hydrogen bond (interaction of the O atom of CO with the hydrogen atom of water). However, for the H_2O-CO system, the interaction can take place through both O and C of CO with the hydrogen atom of H_2O[94]. We have considered both types of interaction and evaluated their effects on the band strengths. However we did not find any significant difference. Thus, we only discuss the band strength of the H_2O-CO mixture with the interaction on the O side of CO. For the sake of completeness, it should be mentioned that there is also another type of interaction, which occurs between the π bond of CO and one water-hydrogen, and it gives rise to a T shaped complex[95]. However, according to a computational study by Collings et

al.[95], this has a negligible effect on IR vibrational bands. As a consequence we have not investigated in detail this kind of complex. The simulated IR absorption spectra of the four fundamental vibrational modes for various compositions are shown in the Appendix (see Figure 17). The four fundamental frequencies of water ice change significantly by increasing the concentration of CO. The most intense peak positions and the corresponding integral abundance coefficients for different H_2O-CO mixtures are provided in the Appendix (see Table 6). In Figure 5d, the integrated intensities of water vibrational modes are plotted as a function of the CO concentration. It is noted that the strength of the libration, bending, and stretching modes decreases with the concentration of CO. The free OH mode shows instead a sharp increase of the band strength when increasing the CO concentration. In Table 4, the resulting linear fit coefficients are collected together with the available experimental values for H_2O-CO mixtures deposited at 15 K.[20] It is noted that theoretical band strength slopes are in rather good agreement with experimental results.[20] For the H_2O-CO system, anharmonic calculations have also been carried out. While the band strengths of the bending and stretching modes have a similar trend as experimental data, a deviation is noted for the libration mode (see Figure 11 in the Appendix).

To check the effect of dispersion, B3LYP-D3/6-31G(d) calculations have been performed, with D3 denoting the correction for dispersion effects[96]. B3LYP-D3 calculations have been carried out for H_2O-CO, H_2O-CH_4, H_2O-N_2, and H_2O-O_2 systems. In Figure 9a, we have shown the comparison of the band strengths of different vibrational modes of water with and without the dispersion correction for the H_2O-CO system. The overall conclusion is that there is a good agreement with the experimental band strengths when dispersion effect is not considered. On the contrary, when the dispersion correction is included, our computed band strength profile shows a different trend. The libration and bending modes present a positive slope with the increase in impurity concentration, whereas experimental results show a negative slope. For the free OH mode, a slight increasing trend of the band strength is obtained, whereas the experimental band strength presents a sharp increase with the

concentration of CO. The band strength of the stretching mode has a similar behaviour with dispersion and without dispersion, and in agreement with the experimental result[20](see Figure 3). Thus, in summary, while we are not claiming that the dispersion effects are not important for the systems investigated, we have noted that neglecting them we obtain a consistent description of the experimental behaviour (probably due to a fortuitous errors compensation).

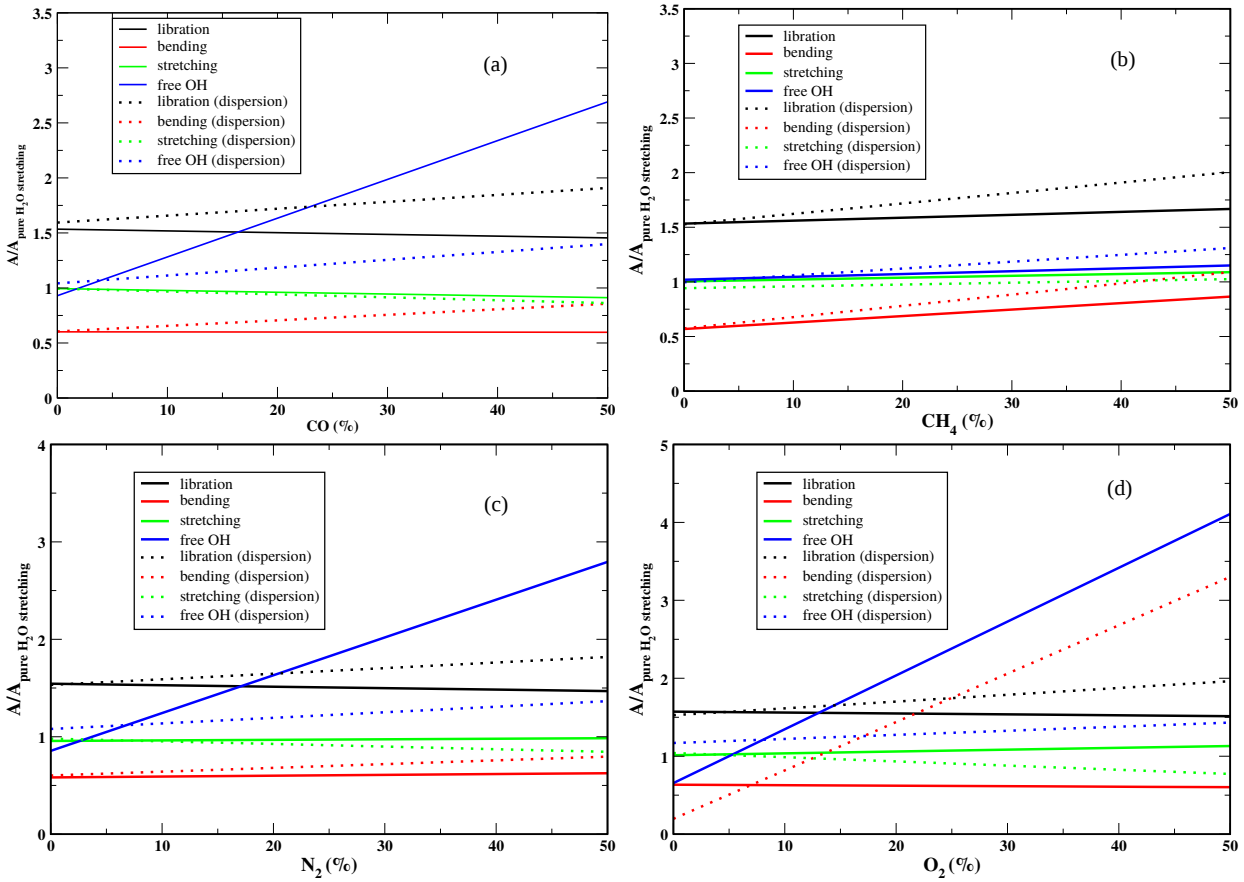

Figure 9: Comparison of the band strengths of the four fundamental modes of water for various mixtures of (a) H_2O-CO, (b) H_2O-CH_4, (c) H_2O-N_2, and (d) H_2O-O_2 by considering or not the dispersion effect.

4.1.7 CO_2 ice

Figure 1f shows the optimized geometry of the 4 : 4 mixture of H_2O:CO_2. The absorption features of water ice for different CO_2 concentrations are shown in the Appendix (see Figure

Table 4: Linear fit coefficients for the $H_2O - X$ (X = HCOOH, NH_3, CH_3OH, CO, CO_2, H_2CO, CH_4, OCS, N_2, and O_2) mixtures.

Mixture	**Vibrational mode**	**Linear coefficients**	
		Constant [10^{-16} cm molecule^{-1}]	**Slope** [10^{-19} cm molecule^{-1}]
H_2O-HCOOH	$\nu_{\text{libration}}$	2.45 (0.26)[a]	132.73 (0.90)[a]
	ν_{bending}	0.58 (0.05)[a]	184.25 (14.40)[a]
	$\nu_{\text{stretching}}$	1.80 (1.90)[a]	48.60 (-7.30)[a]
	$\nu_{\text{free-OH}}$	0.20 (0.16)[a]	9.80 (-0.40)[a]
H_2O-NH_3	$\nu_{\text{libration}}$	0.27 (0.34)[a]	6.11 (5.00)[a]
	ν_{bending}	0.09 (0.12)[a]	5.48 (2.20)[a]
	$\nu_{\text{stretching}}$	1.90 (2.38)[a]	0.41 (-14.4)[a]
	$\nu_{\text{free-OH}}$	0.21 (0.12)[a]	-4.21 (-2.1)[a]
H_2O-CH_3OH	$\nu_{\text{libration}}$	0.25	10.0
	ν_{bending}	0.12	2.00
	$\nu_{\text{stretching}}$	1.92	32.00
	$\nu_{\text{free-OH}}$	0.26	2.65
H_2O-CO	$\nu_{\text{libration}}$	0.30 (0.30±0.02) [20]	-0.32 (-2.1±0.4) [20]
	ν_{bending}	0.12 (0.13±0.02) [20]	-0.016 (-1.0 ±0.3) [20]
	$\nu_{\text{stretching}}$	1.98 (2.0±0.1) [20]	-3.2 (-16±3) [20]
	$\nu_{\text{free-OH}}$	0.18 (0.0) [20]	5.69 (1.2 ±0.1) [20]
H_2O-CO_2	$\nu_{\text{libration}}$	0.3 (0.32±0.02) [21]	2.07 (-3.2±0.4) [21]
	ν_{bending}	0.11 (0.14±0.01) [21]	0.12 (-0.5±0.2) [21]
	$\nu_{\text{stretching}}$	2.02 (2.1±0.1) [21]	-0.22 (-22±2) [21]
	$\nu_{\text{free-OH}}$	0.19 (0.0) [21]	10.02 (1.62±0.07) [21]
H_2O-H_2CO	$\nu_{\text{libration}}$	0.26	5.73
	ν_{bending}	0.10	4.59
	$\nu_{\text{stretching}}$	1.92	0.10
	$\nu_{\text{free-OH}}$	0.13	16.53
H_2O-CH_4	$\nu_{\text{libration}}$	0.31	0.53
	ν_{bending}	0.11	1.18
	$\nu_{\text{stretching}}$	2.01	3.39
	$\nu_{\text{free-OH}}$	0.20	0.52
H_2O-OCS	$\nu_{\text{libration}}$	0.30	0.42
	ν_{bending}	0.11	0.23
	$\nu_{\text{stretching}}$	1.96	2.18
	$\nu_{\text{free-OH}}$	0.17	0.13
H_2O-N_2	$\nu_{\text{libration}}$	0.31	-0.30
	ν_{bending}	0.12	0.17
	$\nu_{\text{stretching}}$	0.12	0.11
	$\nu_{\text{free-OH}}$	0.17	7.75
H_2O-O_2	$\nu_{\text{libration}}$	0.31	-0.23
	ν_{bending}	0.12	-0.13
	$\nu_{\text{stretching}}$	2.02	4.71
	$\nu_{\text{free-OH}}$	0.13	13.80

Notes. Experimental values are provided in the parentheses. [a]This work.

18). The most intense frequencies for the various H_2O-CO_2 mixtures are summarized in the Appendix as well (see Table 6). The trend of the band strength as a function of CO_2 concentrations is shown in Figure 5e. For the free-OH mode, a rapid increase with CO_2 concentration is noted, which is in good agreement with the experimental results by Öberg et al.[21]. Computed band strengths of the libration and bending modes also increase by increasing the CO_2 concentration, which is however in contrast with the available experimental data.[21] The band strength of the bulk stretching mode decreases instead with CO_2 concentration, in reasonable good agreement with the available experiments.[21] FTIR spectroscopy of the matrix-isolated molecular complex H_2O-CO_2 shows that CO_2 does not form a weak hydrogen bond with H_2O,[97] but instead CO_2 destroys the bulk hydrogen bond network. This may cause a large decrease in the band strength of the bulk stretching mode, while the intermolecular O-H bond strength increases with the CO_2 concentration. Therefore, the disagreement between calculated and experimental band strengths could be thus due to the cluster size of water molecules. In Table 4, the resulting linear fit coefficients are reported, together with the available experimental values for the H_2O-CO_2 mixture deposited at 15 K.[21]

4.2 Part 2. Applications

The results discussed in previous sections suggest that the water c-tetramer structure together with harmonic B3LYP/6-31G(d) calculations are able to predict the experimental results presented here as well as literature data. Thus, to study the effect of other impurities (H_2CO, CH_4, OCS, N_2, and O_2) on pure water ice, we have further exploited this methodology. Additionally, the effect of impurities on the band strengths of the four fundamental bands has also been studied by considering the c-hexamer (chair) structure and the corresponding results are provided in the Supporting Information (see Figure S2).

4.2.1 H_2CO ice

The strongest modes of formaldehyde (H_2CO) lie at 1724.14 cm^{-1} (5.80 μm) and 1497.01 cm^{-1} (6.68 μm). Figure 1g depicts the optimized structure of the $4:4$ $H_2O - H_2CO$ mixture. The desired ratio is attained upon formation of the hydrogen bond between the O atom of H_2CO and the dangling H atoms of H_2O. The effect of formaldehyde on water IR spectrum is shown in the Appendix (see Figure 19). Frequencies, integral absorption coefficients, and mode assignments are reported in the Appendix as well (see Table 6). The band strength profiles as a function of the concentration of H_2O are shown in Figure 5f. Similar to the methanol-water mixture, all band strengths are found to increase with the concentration of formaldehyde, the free-OH stretching mode being the most affected.

4.2.2 CH_4 ice

CH_4 cannot be observed by means of rotational spectroscopy since it has no permanent dipole moment. The optimized structure of the $H_2O - CH_4$ system with a $4:4$ ratio is shown in Figure 1h. The absorption IR spectra for different $H_2O - CH_4$ mixtures are depicted in the Appendix (see Figure 20). Peak positions, integral absorption coefficients, and band assignments are provided in the Appendix as well (see Table 6). Figure 5g shows the band strength variations with the concentration of CH_4. All band strengths marginally increase with the CH_4 concentration. Figure 9b shows the comparison of the band strengths with and without the incorporation of corrections for accounting for dispersion effects. For all the four fundamental modes, differences are minor.

4.2.3 OCS ice

Garozzo et al.[98] proposed that carbonyl sulfide (OCS) is a key ingredient of the grain surface. Its abundance in ice phase may vary between 0.05 and 0.15%.[16] Figure 1i shows the optimized structure of the 4:4 H_2O-OCS. Since oxygen is more electronegative than sulfur, the O atom of the OCS molecule is hydrogen-bonded to the water free-hydrogens. In the Appendix, Figure

21 shows the absorption IR band spectra for H_2O-OCS clusters with various concentrations. Figure 5h depicts the band strengths as a function of the concentration of OCS. Here, the free-OH mode is the most affected and its band strength increases with the concentration of OCS. All other modes roughly remain invariant by varying the amount of impurity.

4.2.4 N_2 ice

N_2 is a stable homonuclear molecule and, due to its symmetry, it is infrared inactive. However, when embedded in an ice matrix, the crystal field breaks the symmetry, and an infrared transition is activated around 2325.58 cm^{-1} (4.30 μm). Figure 1j shows the optimized geometry of the H_2O-N_2 system with a 4 : 4 ratio. The IR absorption spectra of water ice containing different amounts of N_2 are shown in the Appendix (see Figure 22). The corresponding peak frequencies and intensities are provided in the Appendix as well (see Table 6). The dependence of the band strengths on the N_2 concentration is depicted in Figure 5i. It has been found that the slope of the band strength of the libration mode decreases, whereas the bending, stretching, and free OH modes show an increasing trend with the concentration of N_2. The linear fitting coefficients are provided in Table 4. Figure 9c shows the comparison of band strengths with and without considering the dispersion effects. It is noted that the inclusion of dispersion effect leads to small changes.

4.2.5 O_2 ice

Analogously to N_2, O_2 is a homonuclear molecule, which is infrared inactive except when it is embedded in an ice matrix,[99,100] thus giving rise to an absorption band around 1550.39 cm^{-1} (6.45 μm). O_2 ice is not much abundant because the largest part of the oxygen budget in the dense molecular clouds is locked in the form of CO_2, CO, water ice, and silicates. The optimized geometry of the 4 : 4 H_2O-O_2 ratio is shown in Figure 1k. IR spectra for different concentrations (Figure 23) and the corresponding peak frequencies and intensities (Table 6) are provided in the Appendix. The dependence of band strengths upon O_2 concentration is

shown in Figure 5j. Similarly to the N_2-water case, the free-OH mode is the most affected. The slope of the band strength of the libration and bending modes decreases, whereas the stretching and free-OH modes show an increasing trend with the concentration of O_2. The fitting coefficients for different H_2O-N_2 mixtures are provided in Table 4.

Figure 9d depicts the comparison of the band strengths with and without the inclusion of dispersion effects for the H_2O-O_2 system. It is evident that trend of the band strength with the impurity concentration slightly increases for the libration mode, whereas slightly decreases for the stretching mode when corrections for dispersion effects are present. In the case of the bending mode, the band strength rapidly increases, whereas the band strength rapidly decreases for the free OH mode.

4.2.6 Comparison between various mixtures

To compare the effect of all impurities considered in this study on the band strength, we have plotted the band profiles of the four fundamental modes of water ice as a function of the concentration of impurities, the results being shown in Figure 10, top panel. For all fundamental modes, band strengths increase with the concentration of CH_3OH, H_2CO, HCOOH, CH_4. To better understand their effect, in Figure 10, bottom panel, we report the relative band strengths for the $4:4$ ratio mixtures. From this, it is clear that the libration, bending, and stretching modes are mostly affected by formic acid, while the free-OH mode is mostly affected by formaldehyde. An interesting feature is found for the free-OH mode for the $NH_3 - H_2O$ system. By increasing the NH_3 concentration with respect to pure water, the band strength of the free-OH mode decreases and disappears when the $4:4$ concentration ratio is reached.

Figure S1 (in the SI) depicts the optimized structures of the pure water c-hexamer (chair) configuration along with those obtained for a 6:1 concentration ratio. Figure S2 collects the results for the band strength variations for the c-hexamer (chair) water cluster configuration is considered, this being analogous to Figure 5. The geometries of water clusters containing

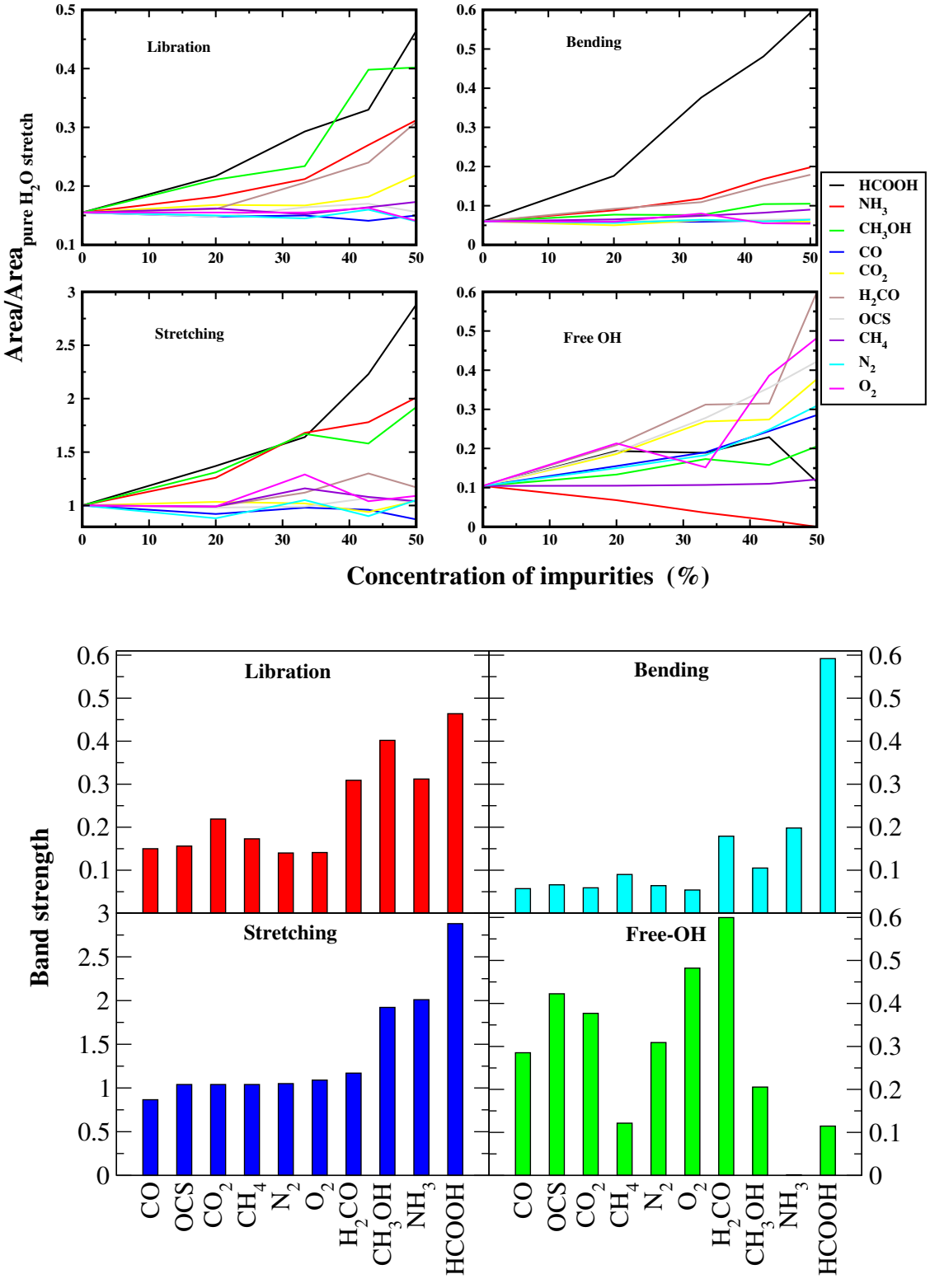

Figure 10: Top panel: Effect of impurities on the four fundamental vibrational modes of water. Bottom panel: Comparison of the band strengths for the four fundamental vibrational modes as affected by impurities.

20 water molecules with HCOOH as an impurity in various concentrations are shown in Figure S3 (in the SI) and the corresponding variations of the band strengths with increasing concentration of HCOOH are depicted in Figure S4 (in the SI). This figure also reports the comparison of band strength profiles for different water clusters. The structures of the 20-water-molecule cluster have been taken from Shimonishi et al.[101], and were obtained by MD-annealing calculations using classical force-fields to reproduce a water cluster as a model of the ASW surface. The comparison shown in Figure S4 demonstrates that the $4H_2O$ model provides results similar to those obtained with 6 and 20 water molecules. This furthermore confirms the validity of our approach.

5 Conclusions

Water ice is known to be the major constituent of interstellar icy grain mantles. Interestingly, there have been several astronomical observations[41,102] of the OH stretching and HOH bending modes at 3278.69 cm^{-1} (3.05 μm) and 1666.67 cm^{-1} (6.00 μm), respectively. It is noteworthy that the intensity ratio of these two bands is very different from what obtained in laboratory experiments for pure water ice. This suggested that the presence of impurities in water ice affects the spectroscopic features of water itself. For this reason, a series of laboratory experiments were carried out in order to explain the discrepancy between observations and experiments. Furthermore, these observations prompted us to perform an extensive computational investigation aiming to evaluate the effect of different amounts of representative impurities on the band strengths and absorption band profiles of interstellar ice. We selected the most abundant impurities (HCOOH, NH_3, CH_3OH, CO, CO_2, H_2CO, CH_4, OCS, N_2, and O_2) and studied their effect on four fundamental vibrational bands of pure water ice by employing different cluster models. Indeed, both the experimental and theoretical peak positions might differ from the astronomical observations. This is because the grain shape, size, and constituents, the sur-

rounding physical conditions, and the presence of impurities play a crucial role in tuning the ice spectroscopic features.

Although most of the computations were performed for a cluster containing only four water molecules as a model system (to find a trend in the absorption band strength), we demonstrated that increasing the size of the cluster would change the band strength profile only marginally. From the band strength profiles shown in Figure S5 (in the SI), it is apparent that the stretching mode is the most affected and the bending mode is the least affected by the presence of impurities. Libration, bending, and bulk stretching modes were found to be most affected by HCOOH impurity, followed by CH_3OH and H_2CO. Another interesting point to be noted is that the band strength of the free-OH stretching mode decreases with increasing concentration of NH_3 and completely vanishes when the concentration of NH_3 becomes 50%. Most interestingly, the experimental free-OH band profile shows a decreasing trend when water is mixed with NH_3 (Figure 7, right panel), similarly to that obtained computationally.

Finally, our computed and laboratory absorption spectra of water-rich ices will be part of a larger infrared ice database in support of current and future observations. Understanding the effect of impurities in interstellar polar ice analogs will be pivotal to support the unambiguous identification of COMs in interstellar ice mantles by using future space missions such as JWST[9].

6 Acknowledgment

PG acknowledges the support of CSIR (Grant No. 09/904(0013) 2K18 EMR-I). MS gratefully acknowledges DST-INSPIRE Fellowship [IF160109] scheme. AD acknowledges ISRO respond (Grant No. ISRO/RES/2/402/16-17). This research was possible in part due to a Grant-

In-Aid from the Higher Education Department of the Government of West Bengal. SI acknowledges the Royal Society for financial support. ZK was supported by VEGA – The Slovak Agency for Science, Grant No. 2/0023/18. This work was also supported by COST Action TD1308 – ORIGINS.

7 Supporting Information (SI)

Optimized structures of water clusters and impurities mixed with a 6:1 concentration ratio (Figure S1); band strengths of the four fundamental vibration modes of water clusters containing impurities with various concentrations (Figure S2); structure of water clusters containing 20 H_2O molecules with HCOOH as impurity in different concentration ratio (Figure S3); comparison of the band strength of various water clusters mixed with HCOOH (Figure S4); effect of the cluster size on the band strength profile (Figure S5); harmonic infrared frequencies and intensities of the $4H_2O$ cluster (Table S1), $4H_2O$/HCOOH (Table S2), $4H_2O$/2HCOOH (Table S3), $4H_2O$/3HCOOH (Table S4), $4H_2O$/4HCOOH (Table S5), $4H_2O/NH_3$ (Table S6), $4H_2O/2NH_3$ (Table S7), $4H_2O/3NH_3$ (Table S8), $4H_2O/4NH_3$ (Table S9) evaluated at the B2PLYP/maug-cc-pVTZ level; harmonic infrared frequencies and intensities of the H_2O^{QM} + 3 H_2O^{MM} complex (Table S10); harmonic infrared frequencies and intensities of the first 4 H_2O^{QM}+16 H_2O^{MM}: complex configuration 1 (Table S11) and complex configuration 2 (Table S12); geometric details of optimized structures of water clusters and impurities mixed with 4:4 and 6:1 concentration ratios (Optimized-Structures.zip). The Supporting Information is available free of charge on the ACS Publications website.

References

(1) Eddington, A. S. Interstellar matter. *The Observatory* **1937**, *60*, 99-103.

(2) Tielens, A. G. G. M.; Hagen, W. Model calculations of the molecular composition of interstellar grain mantles. *Astron. Astrophys.* **1982**, *114*, 245.

(3) Woon, D. Pathways to glycine and other amino acids in ultraviolet-irradiated astrophysical ices determined via quantum chemical modeling. *Astrophys. J. Lett.* **2002**, *571*, L177.

(4) Nuevo, M.; Sandford, S.A. The photochemistry of pyrimidine in realistic astrophysical ices and the production of nucleobases. *Astrophys. J.* **2014**, *793*, 125.

(5) Das, A.; Acharyya, K.; Chakrabarti, S.; Chakrabarti, S. K. Formation of water and methanol in star forming molecular clouds. *Astron. Astrophys.* **2008**, *486*, 209-220.

(6) Das, A.; Acharyya, K; Chakrabarti, S. K. Effects of initial condition and cloud density on the composition of the grain mantle. *Mon. Not. R. Astron. Soc.* **2010**, *409*, 789-800.

(7) Das, A.; Chakrabarti, S. K. Composition and evolution of interstellar grain mantle under the effects of photodissociation. *Mon. Not. R. Astron. Soc.* **2011**, *418*, 545-555.

(8) Das, A.; Sahu, D.; Majumdar, L.; Chakrabarti, S. K. Deuterium enrichment of the interstellar grain mantle. *Mon. Not. R. Astron. Soc.* **2016**, *455*, 540-551.

(9) Gibb, E. L.; Whittet, D. C. B.; Boogert, A. C. A.; Tielens, A. G. G. M. Interstellar ice: the infrared space observatory legacy. *Astrophys. J., Suppl. Ser.* **2004**, *151*, 35.

(10) Whittet, D. C. B. *Dust in the Galactic Environment*; 2nd ed.; Bristol: Institute of Physics (IOP) Publishing, 2003; Series in Astronomy and Astrophysics.

(11) Gillett. F. C.; Forrest. W. J. Spectra of the Becklin-Neugebauer point source and the Kleinmann-Low nebula from 2.8 to 13.5 microns. *Astrophys. J.* **1973**, *179*, 483-491.

(12) Irvine, W. M.; Pollack, J. B. Infrared optical properties of water and ice spheres. *Icarus* **1968**, *8*, 324-360.

(13) Merrill, K. M.; Russell, R. W.; Soifer, B. T. Infrared observations of ices and silicates in molecular clouds. *Astrophys. J.* **1976**, *207*, 763-769.

(14) Leger, A.; Klein, J.; de Cheveigne, S.; Guinet, C.; Defourneau, D.; Belin, M. *Astron. Astrophys.* **1979**, *79*, 256-259.

(15) Hagen, W.; Allamandola, L.; Greenberg, J. M. Interstellar molecule formation in grain mantles: The laboratory analog experiments, results and implications. *Astrophys. Space Sci.* **1979**, *65*, 215-240.

(16) Dartois, E. *The ice survey opportunity of ISO;* In ISO Science Legacy. Springer: Dordrecht, **2005**, *119*, 293-310.

(17) van Dishoeck, E. F.; Blake, C. A.; Draine B. T.; Lunine, J. I. The Chemical Evolution of Protostellar and Protoplanetary Matter. In *Protostars and Planets III*, Levy, E. H., Lunine, J. I., Eds.; ISBN 0-8165-1334-1. LC QB806 .P77; University of Arizona Press: Tucson, Arizona, 1993; 163-241.

(18) Boogert, A. C. Adwin; Gerakines, Perry A.; Whittet, Douglas C. B. Observations of the Icy Universe. *Annual Review of Astronomy and Astrophysics* **2015**, *53*, 541-581.

(19) Ohno, K.; Okimura, M.; Akaib, N.; Katsumotoa, Y. The effect of cooperative hydrogen bonding on the OH stretching-band shift for water clusters studied by matrix-isolation infrared spectroscopy and density functional theory. *Phys. Chem. Chem. Phys.* **2005**, *7*, 3005-3014.

(20) Bouwman, J.; Ludwig, W.; Awad, Z.; Öberg, K.L.; Fuchs, G. W.; van Dishoeck, E. F.; Linnartz, H. Band profiles and band strengths in mixed H2O:CO ices. *Astron. Astrophys.* **2007**, *476*, 995.

(21) Öberg, K. I.; Fraser, H.J.; Boogert, A. C. A.; Bisschop, S. E.; Fuchs, G. W.; van

Dishoeck, E. E.; Linnartz, H. Effects of CO2 on H2O band profiles and band strengths in mixed H2O: CO2 ices. *Astron. Astrophys.* **2007**, *462*, 1187.

(22) Gerakines, P. A.; Schutte, W. A.; Greenberg, J. M.; van Dishoeck, E. F. The infrared band strengths of H_2O, CO and CO_2 in laboratory simulations of astrophysical ice mixtures. *Astron. Astrophys.* **1995**, *296*, 810.

(23) Ehrenfreund, P.; Boogert, A. C. A.; Gerakines, P. A.; Tielens, A. G. G. M.; van Dishoeck, E. F. Infrared spectroscopy of interstellar apolar ice analogs. *Astron. Astrophys* **1997**, *328*, 649-669.

(24) Schutte, W. A.; Boogert, A. C. A.; Tielens, A. G. G. M.; Whittet, D. C. B.; Gerakines, P. A.; Chiar, J. E.; Ehrenfreund, P.; Greenberg, J. M.; van Dishoeck, E. F.; Graauw, T. Weak ice absorption features at 7.24 and 7.41 μm in the spectrum of the obscured young stellar object W 33A. *Astron. Astrophys* **1999**, *343*, 966.

(25) Cooke, I. R.; Fayolle, E.C.; Öberg, K. I. CO_2 Infrared Phonon Modes in Interstellar Ice Mixtures. *Astrophys. J.* **2016**, *832*, 5.

(26) Soifer, B. T.; Puetter, R. C.; Russell, R. W.; Willner, S. P.; Harvey, P. M.; Gillett, F. C. The 4-8 micron spectrum of the infrared source W33 A. *Astrophys. J. Lett.* **1979** *232*, L53-L57.

(27) Mantz, A. W.; Maillard, J. P.; Roh, W. B.; Narahari Rao, K. Ground state molecular constants of $^{12}C^{16}O$. *J. Mol. Spectrosc.* **1975**, *57*, 155.

(28) Chiar, J. E.; Whittet, D. C. B.; Adamson, A. J.; Kerr, T. H. Ices in the Taurus dark cloud environment. In *From Gas to Stars to Dust*; Haas, M. R., Davidson, J. A., Erickson, E. F., Eds.; Astronomical Society of the Pacific Conference Series, 1995; Vol. 73, pp 75-78.

(29) Chiar, J. E.; Gerakines, P. A.; Whittet, D. C. B.; Pendleton, Y.; Tielens, A. G. G. M.; Adamson, A. J.; Boogert, A. C. A. Processing of icy mantles in protostellar envelopes. *Astrophys. J.* **1998**, *498*, 716.

(30) D'Hendecourt, L.B.; Jourdain de Muizon, M. The discovery of interstellar carbon dioxide. *Astron. Astrophys.* **1989**, *223*, L5.

(31) de Graauw, T., Whittet, D.C.B., Gerakines, P.A., et al. SWS observations of solid CO_2 in molecular clouds. *Astron. Astrophys.* **1996**, *315*, L345.

(32) Guertler, J.; Henning, T.; Koempe, C.; Pfau, W.; Kraetschmer, W.; Lemke, D. Detection of solid CO_2 towards young stellar objects. *Astronomische Gesellschaft Abstract Series* **1996**, *12*, 107.

(33) Gerakines, P. A.; Whittet, D. C. B.; Ehrenfreund, P.; Boogert, A. C. A.; Tielens, A. G. G. M.; Schutte, W. A.; Chiar, J.E.; van Dishoeck, E. F.; Prusti, T.; Helmich, F. P.; De Graauw, T. Observations of solid carbon dioxide in molecular clouds with the infrared space observatory. *Astrophys. J.* **1999**, *522*, 357.

(34) Gibb, E. L.; Whittet, D. C. B.; Schutte, W. 8.; Boogert, A. C. A.; Chiar, J. E.; Ehrenfreund, P.; Gerakines, P. A.; Keane, J. V.; Tielens, A. G. G. M.; van Dishoeck, E. F.; Kerkhof, O. An inventory of interstellar ices toward the embedded protostar W33A. *Astrophys. J.* **2000**, *539*, 347.

(35) Baas, F.; Grim, R. J. A.; Geballe, T. R.; Schutte, W.; Greenberg, J. M. *The detection of solid methanol in W33A*; Dust in the Universe, 1988; 55-60.

(36) Grim, R. J. A.; Bass, F.; Geballe, T. R.; Greenberg, J. M.; Schutte, W. Detection of solid methanol toward W33A. *Astron. Astrophys.* **1991**, *243*, 473.

(37) Allamandola, L. J.; Sandford, S. A.; Tielens, A. G. G. M.; Herbst, T. M. Infrared spec-

troscopy of dense clouds in the CH stretch region-Methanol and 'diamonds'. *Astrophys. J.* **1992**, *399*, 134-146.

(38) Schutte, W. A.; Gerakines, P. A.; Geballe, T. R.; van Dishoeck, E. F.; Greenberg, J. M. Discovery of solid formaldehyde toward the protostar GL 2136: observations and laboratory simulation. *Astron. Astrophys.* **1996**, *309*, 633.

(39) Kessler, M. F.; Steinz, J. A.; Anderegg, M. E.; Clavel, J.; Drechsel, G.; Estaria, P.; Faelker, J.; Riedinger, J. R.; Robson, A.; Taylor, B. G.; Ximénez de Ferrán, S. The Infrared Space Observatory (ISO) mission. *Astron. Astrophys.* **1996**, *315*, L27-L31.

(40) Kessler, M. F.; Mueller, T. G.; Leech, K.; Arviset, C.; Garcia-Lario, P.; Metcalfe, L.; Pollock, A.; Prusti, T.; Salama, A. In *The ISO Handbook, Volume I: ISO - Mission & Satellite Overview*, Version 2.0; Mueller, T. G., Blommaert, J. A. D. L., Garcia-Lario, P., Eds.; ESA SP-1262, ISBN No. 92-9092-968-5, ISSN 0379-6566; Eur. Space Agency, 2003; 92.

(41) Keane, J. V.; Boogert, A. C. A.; Tielens, A. G. G. M.; Ehrenfreund, P.; Schutte, W. A. Bands of solid CO_2 in the 2-3 μm spectrum of S 140: IRS1. *Astron. Astrophys.* **2001**, *375*, L43-L46.

(42) van Dishoeck, E. F.; Blake, G. A.; Jansen, D. J.; Groesbeck, T. D. Molecular abundances and low mass star formation II. Organic and deuterated species towards IRAS 16293-2422. *Astrophys. J.* **1995**, *447*, 760-782.

(43) Ikeda, M.; Ohishi, M.; Nummelin, A.; Dickens, J. E.; Bergman, P.; Hjalmarson, *Å*.; Irvine, W. M. Survey observations of $c-C_2H_4O$ and CH_3CHO toward massive star-forming regions. *Astrophys. J.* **2001**, *560*, 792.

(44) Lacy, J. H.; Carr, J. S.; Evans, N. J.; Baas, F.; Achtermann, J. M.; Arens, J. F. *Astrophys. J.* **1991**, *376*, 556-560.

(45) Öberg, K. I.; Boogert, A. C. A.; Pontoppidan, K. M.; Blake, G. A.; Evans, N. J.; Lahuis, F.; van Dishoeck, E. F. The c2d spitzer spectroscopic survey of ices around low-mass young stellar objects. III. CH_4. *Astrophys. J.* **2008**, *678*, 1032.

(46) Knacke, R. F.; McCorkle, S.; Puetter, R. C.; Erickson, E. F.; Kraetschmer, W. Observation of interstellar ammonia ice. *Astrophys. J.* **1982**, *260*, 141-146.

(47) Knacke, R. F.; McCorkle, S.M. Spectroscopy of the Kleinmann-Low nebula-Scattering in a solid absorption band. *Astron. J.* **1987**, *94*, 972-976.

(48) Lacy, J. H.; Faraji, H.; Sandford, S. A.; Allamandola, L. J. Unraveling the 10 micron "silicate" feature of protostars: the detection of frozen interstellar ammonia. *Astrophys. J. Lett.* **1998**, *501*, L105.

(49) Palumbo, M. E.; Tielens, A. G. G. M.; Tokunaga, A. T. Solid carbonyl sulphide (OCS) in W33A. *Astrophys. J.* **1995**, *449*, 674-680.

(50) Palumbo, M. E.; Geballe T. R.; Tielens, A. G. G. M. Solid carbonyl sulfide (OCS) in dense molecular clouds. *Astrophys. J.* **1997**, *479*, 839.

(51) Bieler, A.; Altwegg, K.; Balsiger, H.; Bar-Nun, A.; Berthelier, J. J.; Bochsler, P.; Briois, C.; Calmonte, U.; Combi, M.; De Keyser, J.; van Dishoeck, E. F. Abundant molecular oxygen in the coma of comet 67P/ChuryumovGerasimenko. *Nature* **2015**, *526*, 678.

(52) Rubin, M.; Altwegg, K.; van Dishoeck, E.F.; Schwehm, G. Molecular oxygen in Oort cloud comet 1P/Halley. *Astrophys. J. Lett.* **2015**, *815*, L11.

(53) Sandford, S. A.; Bernstein, M. P.; Allamandola, L. J.; Goorvitch, D.; Teixeira, T. C. V. S. The abundances of solid N2 and gaseous CO2 in interstellar dense molecular clouds. *Astrophys. J.* **2001**, *548*, 836.

(54) Herbst, E.; van Dishoeck, E. F. Complex organic interstellar molecules. *Annu. Rev. Astron. Astrophys.* **2009**, *47*, 427.

(55) Sandford, S. A.; Bernstein, M. P.; Swindle, T. D. The Trapping of Noble Gases by the Irradiation and Warming of Interstellar Ice Analogs. *Meteorit. Planet. Sci.* **1988**, *33*, A135.

(56) Knez, C.; Boogert, A. C. A.; Pontoppidan, K. M.; Kessler-Silacci, J.; van Dishoeck, E. F.; Evans, Neal J., II; Augereau, J-C.; Blake, G. A.; Lahuis, F. Spitzer Mid-Infrared Spectroscopy of Ices toward Extincted Background Stars. *Astrophys. J.* **2005**, *635*, L145-L148.

(57) Choi, J. H.; Cho, M. Vibrational solvatochromism and electrochromism of infrared probe molecules containing C≡O, C≡N, C=O, or C-F vibrational chromophore. *J. Chem. Phys.* **2011** *134*, 154513.

(58) Cappelli, C.; Lipparini, F.; Bloino, J.; Barone, V. Towards an accurate description of anharmonic infrared spectra in solution within the polarizable continuum model: Reaction field, cavity field and nonequilibrium effects. *J. Chem. Phys.* **2011** *135*, 104505.

(59) Błasiak, B.; Lee, H.; Cho, M. Vibrational solvatochromism: Towards systematic approach to modeling solvation phenomena. *J. Chem. Phys.* **2013** *139*, 044111.

(60) Max, J-J.; Chapados, C. Infrared spectroscopy of acetone-water liquid mixtures. I. Factor analysis. *J. Chem. Phys.* **2003**, *119*, 5632.

(61) Max, J-J.; Chapados, C. Infrared spectroscopy of acetone-water liquid mixtures II. Molecular model. *J. Chem. Phys.* **2004**, *120*, 6625.

(62) Jenniskens, P.; Blake, D. F. Structural transitions in amorphous water ice and astrophysical implications. *Science* **1994**, *265*, 753.

(63) Pradzynski, C. C.; Forck, R. M.; Zeuch, T.; Slavíček, P.; Buck, U. A Fully Size-Resolved Perspective on the Crystallization of Water Clusters. *Science* **2012**, *337*, 1529.

(64) Odutola, J. A.; Dyke, T. R. Partially deuterated water dimers: Microwave spectra and structure. *J. Chem. Phys.* **1980**, *72*, 5062.

(65) Viant, M. R.; Cruzan, J. D.; Lucas, D. D.; Brown, M. G.; Liu, K; Saykally, R. J. Pseudorotation in Water Trimer Isotopomers Using Terahertz Laser Spectroscopy. *J. Phys. Chem. A* **1997**, *101*, 9032.

(66) Liu, K.; Brown, M. G.; Saykally, R. J. Terahertz Laser Vibration-Rotation Tunneling Spectroscopy and Dipole moment of cage Form of the Water Hexame. *J. Phys. Chem. A*, **1997**, *101*, 8995.

(67) Nauta, K.; Miller, R. E. Formation of Cyclic Water Hexamer in Liquid Helium: The Smallest Piece of Ice. *Science* **2000**, *287*, 293.

(68) Abascal, J.L.F., Sanz, E., Garcia Fernandez, R., Vega, C., *J. Chem. Phys.*, **2005**, 122, 234511.

(69) Sil, M.; Gorai, P.; Das, A.; Sahu, D.; Chakrabarti, S. K. Adsorption Energies of H and H_2: A Quantum Chemical Study. *Eur. Phys. J. D* **2017**, *71*, 45.

(70) Das, A.; Sil, M.; Gorai, P.; Chakrabarti, S. K.; Loison, J-C. An Approach to Estimate the Binding Energy of Interstellar Species. *Astrophys. J. S. S.* **2018**, *237*, 9.

(71) Nguyen, T.; Talbi, D.; Congiu, E.; Baouche, ES.; Loison, J-C.; Dulieu, F. Experimental and Theoretical Study of the Chemical Network of the Hydrogenation of NO on Interstellar Dust Grains. *ACS Earth Space Chem.* **2019**, *3*, 1196.

(72) Puzzarini, C.; Ali, A.; Biczysko, M.; Barone, V. Accurate spectroscopic characterization of protonated oxirane: a potential prebiotic species in titan's atmosphere. *Astrophys. J.* **2014** *792*, 118.

(73) Barone, B.; Biczysko, B.; Puzzarini, C. Quantum Chemistry Meets Spectroscopy for

Astrochemistry: Increasing Complexity toward Prebiotic Molecules. *Acc. Chem. Res.* **2015a**, *48*, 1413.

(74) Becke, A. D. Density-functional exchange-energy approximation with correct asymptotic behavior. *Phys. Rev. A* **1988** *38*, 3098.

(75) Lee, C.; Yang, W.; Parr, R. G.; Development of the Colle-Salvetti correlation-energy formula into a functional of the electron density, *Phys. Rev. B* **1988** *37*, 785.

(76) Frisch, M. J.; Trucks, G. W.; Schlegel, H. B.; Scuseria, G. E.; Robb, M. A.; Cheeseman, J. R.; Scalmani, G.; Barone, V.; Mennucci, B.; Petersson, G. A.; Nakatsuji, H. ; Caricato, M.; Li, X.; Hratchian, H. P.; Izmaylov, A. F.; Bloino, J.; Zheng, G.; Sonnenberg, J. L.; Hada, M.; Ehara, M.; Toyota, K.; Fukuda, R.; Hasegawa, J.; Ishida, M.; Nakajima, T.; Honda, Y.; Kitao, O.; Nakai, H.; Vreven, T.; Montgomery, J. A., Jr.; Peralta, J. E.; Ogliaro, F.; Bearpark, M. J.; Heyd, J. J.; Brothers, E. N.; Kudin, K. N.; Staroverov, V. N.; Keith, T. A.; Kobayashi, R.; Normand, J.; Raghavachari, K.; Rendell, A. P.; Burant, J. C.; Iyengar, S. S.; Tomasi, J.; Cossi, M.; Rega, N.; Millam, J. M.; Klene, M.; Knox, J. E.; Cross. J. B.; Bakken, V.; Adamo, C.; Jaramillo, J.; Gomperts, R.; Stratmann, R. E.; Yazyev, O.; Austin, A. J.; Cammi, R.; Pomelli, C.; Ochterski, J. W.; Martin, R. L.; Morokuma, K.; Zakrzewski, V. G.; Voth, G. A.; Salvador, P.; Dannenberg, J. J.; Dapprich, S.; Daniels, A. D.; Farkas, O.; Foresman, J. B.; Ortiz, J. V.; Cioslowski, J.; Fox, D. J. Gaussian 09, Revision D.01; Gaussian, Inc.: Wallingford CT, 2013.

(77) Grimme, S. J. Semiempirical hybrid density functional with perturbative second-order correlation. *J. Chem. Phys.* **2006**, *124*, 034108.

(78) Papajak E.; Leverentz, H.R.; Zheng, J.; Truhlar, D. G. Efficient Diffuse Basis Sets: cc-pVxZ+ and maug-cc-pVxZ. *J. Chem. Theory Comput.* **2009**, *5*, 1197.

(79) Biczysko, M.; Panek, P.; Scalmani, G.; Bloino, J.; Barone, V. Harmonic and Anhar-

monic Vibrational Frequency Calculations with the Double-Hybrid B2PLYP Method: Analytic Second Derivatives and Benchmark Studies. *J. Chem. Theory Comput.* **2010**, *6*, 2115.

(80) Frisch, M. J.; Trucks, G. W.; Schlegel, H. B.; Scuseria, G. E.; Robb, M. A.; Cheeseman, J. R.; Scalmani, G.; Barone, V.; Petersson, G. A.; Nakatsuji, H.; Li, X.; Caricato, M.; Marenich, A. V.; Bloino, J.; Janesko, B. G.; Gomperts, R.; Mennucci, B.; Hratchian, H. P.; Ortiz, J. V.; Izmaylov, A. F.; Sonnenberg, J. L.; Williams-Young, D.; Ding, F.; Lipparini, F.; Egidi, F.; Goings, J.; Peng, B.; Petrone, A.; Henderson, T.; Ranasinghe, D.; Zakrzewski, V. G.; Gao, J.; Rega, N.; Zheng, G.; Liang, W.; Hada, M.; Ehara, M.; Toyota, K.; Fukuda, R.; Hasegawa, J.; Ishida, M.; Nakajima, T.; Honda, Y.; Kitao, O.; Nakai, H.; Vreven, T.; Throssell, K.; Montgomery, J. A., Jr.; Peralta, J. E.; Ogliaro, F.; Bearpark, M. J.; Heyd, J. J.; Brothers, E. N.; Kudin, K. N.; Staroverov, V. N.; Keith, T. A.; Kobayashi, R.; Normand, J.; Raghavachari, K.; Rendell, A. P.; Burant, J. C.; Iyengar, S. S.; Tomasi, J.; Cossi, M.; Millam, J. M.; Klene, M.; Adamo, C.; Cammi, R.; Ochterski, J. W.; Martin, R. L.; Morokuma, K.; Farkas, O.; Foresman, J. B.; Fox, D. J. Gaussian 16, Revision A.03; Gaussian, Inc.: Wallingford CT, 2016.

(81) Barone, V.; Biczysko, M.; Bloino, J.; Cimino, P.; Penocchio, E.; Puzzarini, C. CC/DFT Route toward Accurate Structures and Spectroscopic Features for Observed and Elusive Conformers of Flexible Molecules: Pyruvic Acid as a Case Study. *J. Chem. Theory Comput.* **2015b**, 11, 4342.

(82) Sanford, S. A.; Nuevo, M.; Bera,P.; Lee, T. J. Prebiotic Astrochemistry and the Formation of Molecules of Astrobiological Interest in Interstellar Clouds and Protostellar Disks. *Chem. Rev.* **2020**, dx.doi.org/10.1021/acs.chemrev.9b00560

(83) Tomasi, J.; Mennucci, B.; Cammi, R. Quantum Mechanical Continuum Solvation Models. *Chem. Rev.* **2005**, *105*, 2999-3094.

(84) Pagliai, M.; Mancini, G.; Carnimeo, I.; De Mitri, N.; Barone, V. Electronic absorption spectra of pyridine and nicotine in aqueous solution with a combined molecular dynamics and polarizable QM/MM approach. *J. Comput. Chem.* **2017**, *38*, 319.

(85) Chung, L. W.; Sameera; W. M. C.; Ramozzi, R.; Page, A .J; Hatanaka, M.; Petrova, G. P.; Harris; T.V.; Li; Xin; K. Z.; Liu, F.; Li, H-B.; Ding, L.; Morokuma; K., The ONIOM Method and Its Applications. *Chem. Rev.* **2015**, *115*, 5678-5796.

(86) Wu, Y.; Tepper, H. L.; Voth, G. A. Flexible simple point-charge water model with improved liquid-state properties. *J. Chem. Phys.* **2006**, *124*, 024503.

(87) Cancés, E.; Mennucci, B.; Tomasi, J. A new integral equation formalism for the polarizable continuum model: Theoretical background and applications to isotropic and anisotropic dielectrics. *J. Chem. Phys.* **1997**, *107*, 3032.

(88) Dawes, A.; Mason, N. J.; Fraser, H. J. Using the C-O stretch to unravel the nature of hydrogen bonding in low-temperature solid methanol-water condensates. *Phys. Chem. Chem. Phys.* **2016**, *18*, 1245-1257.

(89) Licari, D.; Baiardi, A.; Biczysko, M.; Egidi, F.; Latouche, C.; Barone, V. Implementation of a graphical user interface for the virtual multifrequency spectrometer: The VMS-Draw tool. *J. Comput. Chem.* **2015**, *36*, 321-334.

(90) Maréchal, Y. IR spectra of carboxylic acids in the gas phase: A quantitative reinvestigation. *J. Chem. Phys.* **1987**, *87*, 6344.

(91) Bisschop, S. E.; Fuchs, G.W.; Boogert, A.C.A.; van Dishoeck, E.F.; Linnartz, H. Infrared spectroscopy of HCOOH in interstellar ice analogues. *Astron. Astrophys.*, **2007**, *470*, 749.

(92) Mastrapa, R. M.; Sandford, S. A.; Roush, T. L.; Cruikshank, D.P.; Dalle Ore, C. M.

Optical constants of amorphous and crystalline H_2O-ice: 2.5-22 μm (4000-455 cm^{-1} optical constants of H_2O-ice. *Astrophys. J.* **2009**, *701*, 1347.

(93) D'Hendecourt, L. B. Ultraviolet Photoprocessing and Infrared Spectroscopy of Laboratory Simulated Grain Mantles. In *Light on Dark Matter*, Israel, F. P., Eds.; Astrophysics and Space Science Library; Springer, Dordrecht: D. Reidel Publishing Co., 1986; 124, 247-252.

(94) Zamirri, L.; Casassa, S.; Rimola, A.; Segado-Centellas, M.; Ceccarelli, C.; Ugliengo, P., IR spectral fingerprint of carbon monoxide in interstellar water-ice models. *Mon. Not. R. Astron. Soc.*, **2018**, *480*, 1427.

(95) Collings, M. P.; Dever, J . W.; McCoustra, R. S; The interaction of carbon monoxide with model astrophysical surfaces. *Phys. Chem. Chem. Phys.*, **2014**, *16*, 3479-3492.

(96) Grimme, S.; Antony, J.; Ehrlich, S.; Krieg, H.; A consistent and accurate ab initio parametrization of density functional dispersion correction (DFT-D) for the 94 elements H-Pu *J. Chem. Phys.* **2010**, *132*, 154104.

(97) Tso, T.L.; Lee, E. K. C. Role of hydrogen bonding studied by the FTIR spectroscopy of the matrix-isolated molecular complexes, dimer of water, water.carbon dioxide, water.carbon monoxide and hydrogen peroxide.n carbon monoxide in solid molecular oxygen at 12-17 K. *J. Phys. Chem.* **1985**, *89*, 1612.

(98) Garozzo, M.; Fulvio, D.; Kanuchova, Z.; Palumbo M. E.; Strazzulla, G. The fate of S-bearing species after ion irradiation of interstellar icy grain mantles. *Astron. Astrophys.*, **2010**, *509*, A67.

(99) Ehrenfreund, P.; Breukers, R.; D'Hendecourt, L.; Greenberg, J. M. On the possibility of detecting solid O2 in interstellar grain mantles. *Astron. Astrophys.* **1992**, *260*, 431-436.

(100) Ehrenfreund, P.; van Dishoeck, E. F. The search for solid O_2 and N_2 with ISO. *Adv. Space Res.* **1998**, 21, 15E.

(101) Shimonishi, T.; Nakatani, N.; Furuya, K.; Hama, T. Adsorption Energies of Carbon, Nitrogen, and Oxygen Atoms on the Low-temperature Amorphous Water Ice: A Systematic Estimation from Quantum Chemistry Calculations. *Astrophys. J.* **2018**, *855*, 27.

(102) Boogert, A. C. A.; Tielens, A. G. G. M.; Ceccarelli, C.; Boonman, A. M. S.; van Dishoeck, E. F.; Keane, J. V.; Whittet, D. C. B.; de Graauw, Th. Infrared observations of hot gas and cold ice toward the low mass protostar Elias 29. *Astron. Astrophys.* **2000**, *360*, 683-698.

Appendix

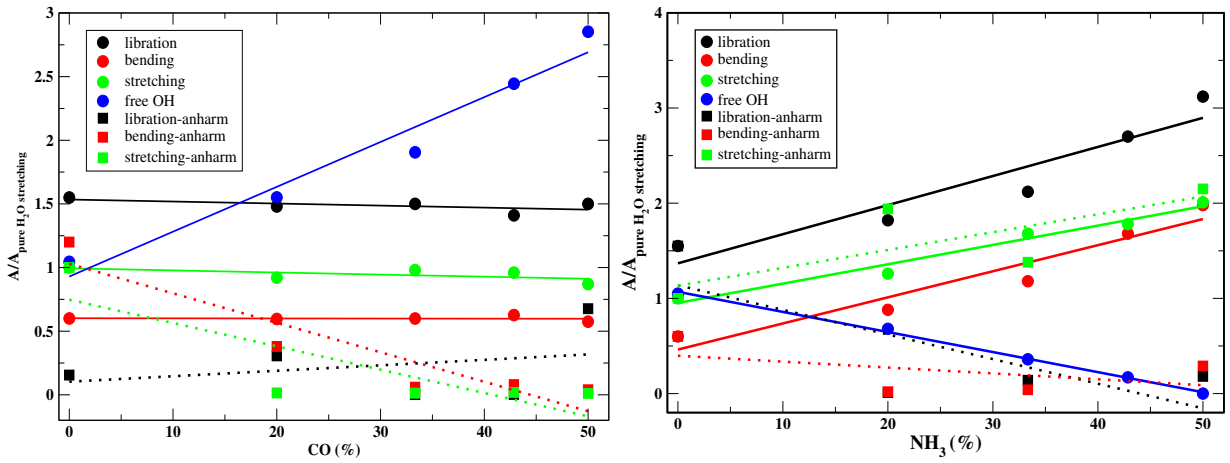

Figure 11: The filled circles are the data points where we considered harmonic frequencies and the corresponding fitted profiles are the solid lines. Solid filled squares represent the data sets where we considered anharmonic frequencies and the corresponding fitted results are the dotted lines.

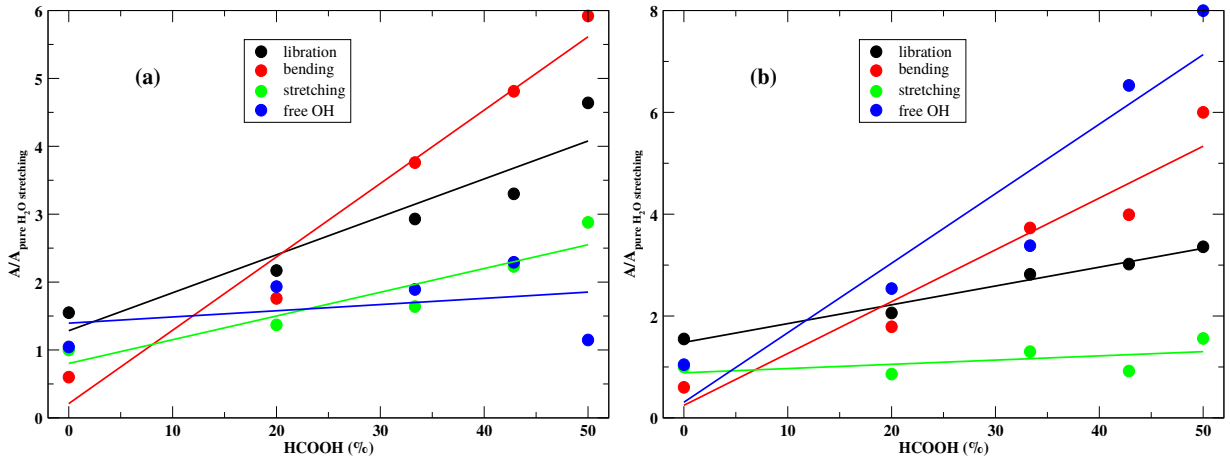

Figure 12: Band strength for H_2O-HCOOH mixtures: (a) HCOOH as hydrogen bond donor, and (b) HCOOH as hydrogen bond acceptor.

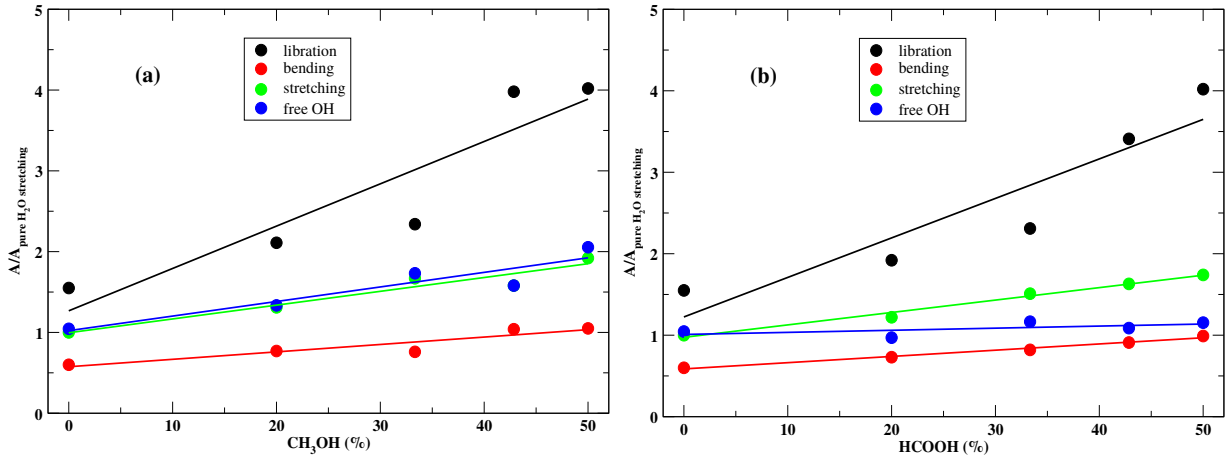

Figure 13: Band strength for H_2O-CH_3OH mixtures: (a) CH_3OH as hydrogen bond donor, and (b) CH_3OH as hydrogen bond acceptor.

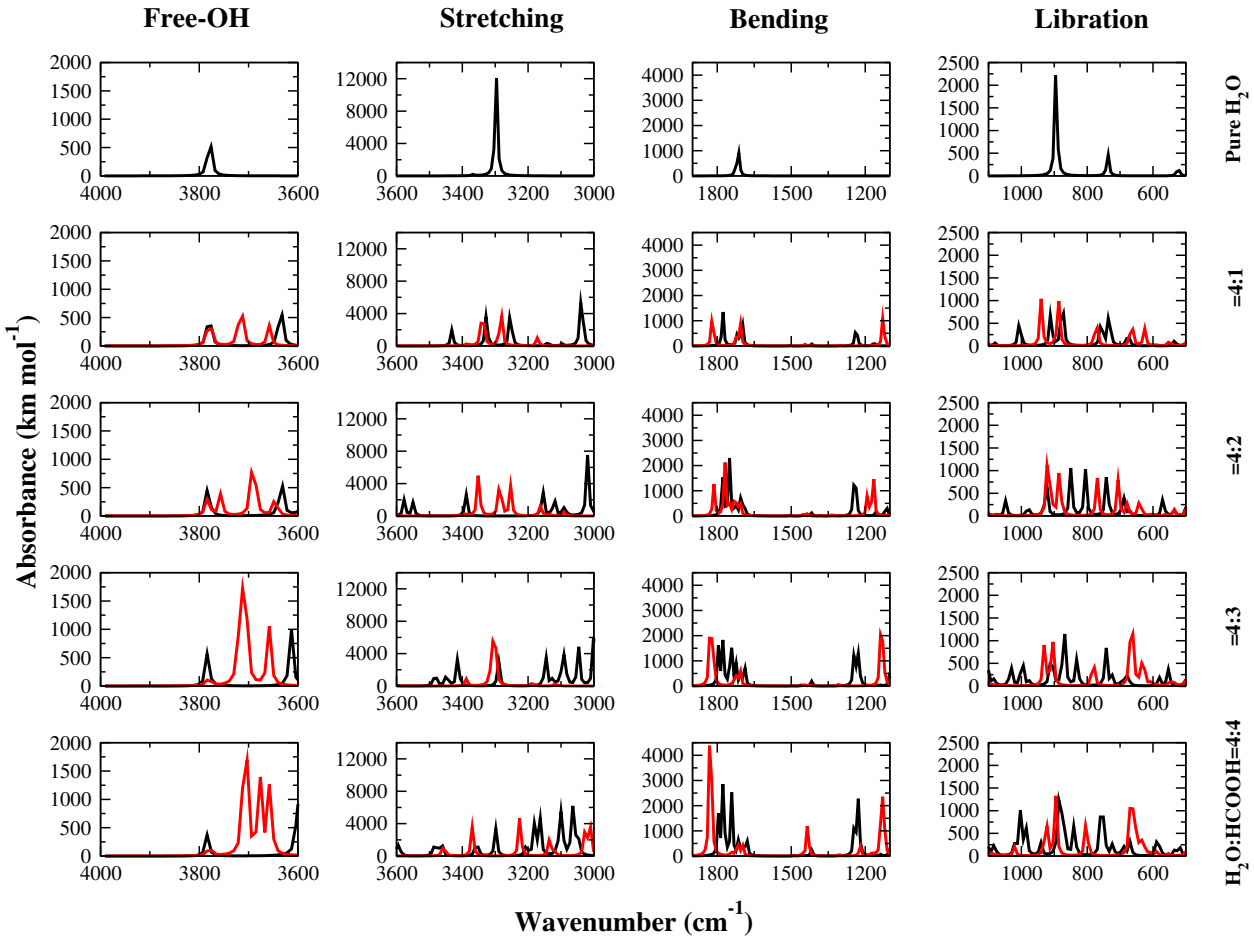

Figure 14: Absorption spectra of the four modes for water ice for the five measured compositions, ranging from pure water ice (top) to 4:4 H_2O-HCOOH mixture (bottom). Black line represent the absorbance spectra of various concentration of H_2O-HCOOH, where HCOOH is used as hydrogen bond donor and for red line HCOOH is used as hydrogen bond acceptor.

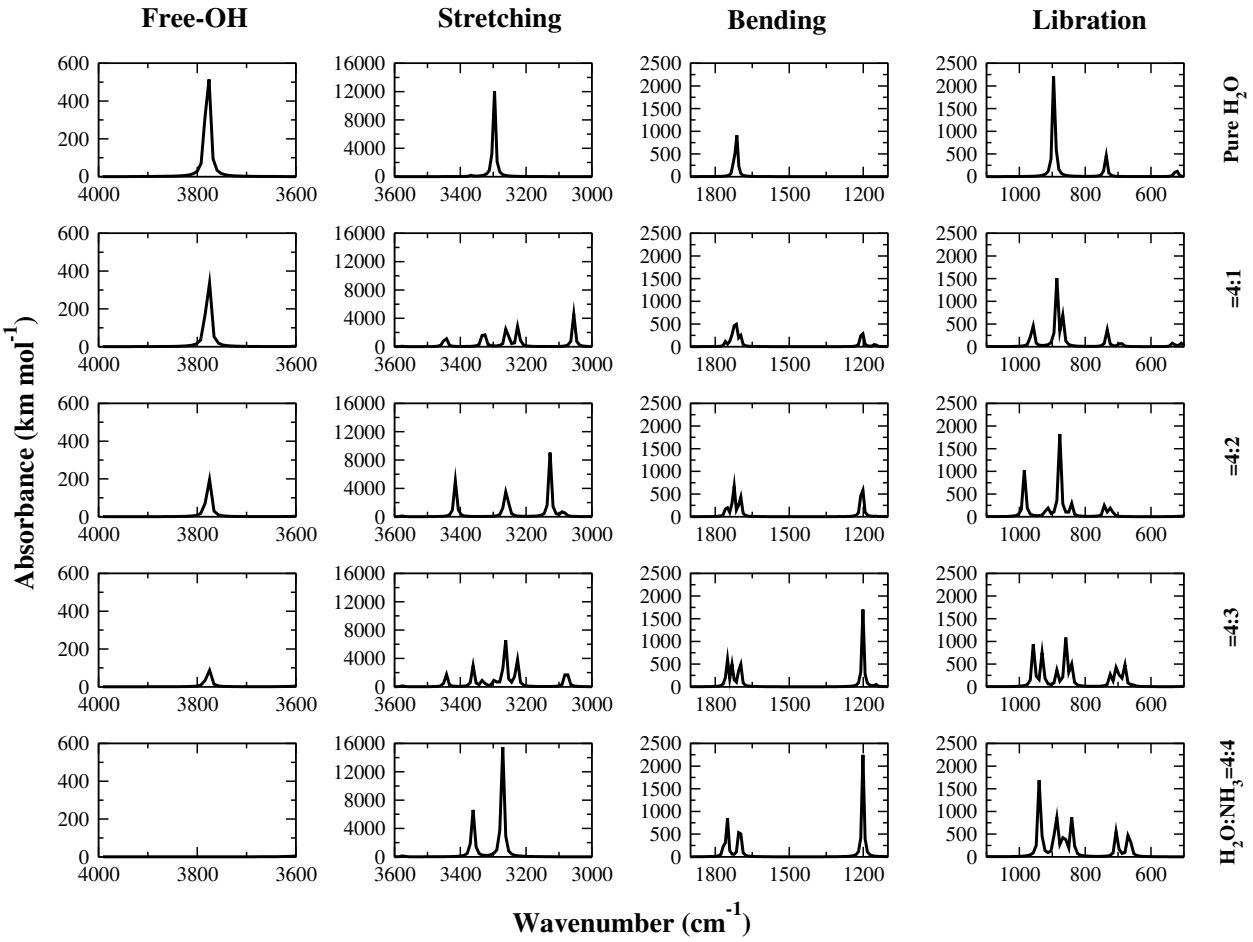

Figure 15: Absorption spectra of the four modes for water ice for the five measured compositions, ranging from pure water ice (top) to 4:4 H_2O-NH_3 mixture (bottom).

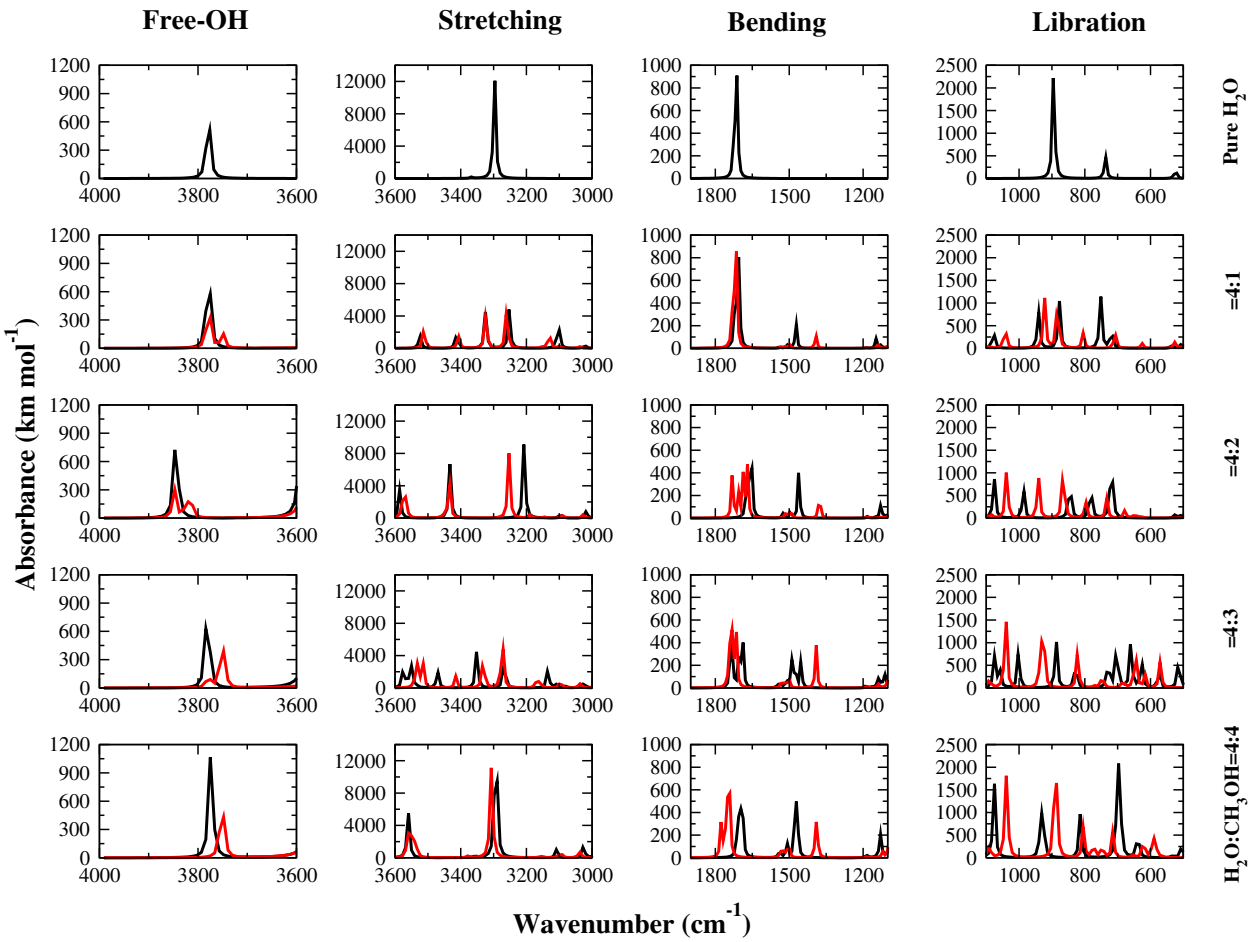

Figure 16: Absorption spectra of the four modes for water ice for the five measured compositions, ranging from pure water ice (top) to 4:4 H_2O-CH_3OH mixture (bottom). Black line represent the absorbance spectra of various concentration of H_2O-CH_3OH, where CH_3OH is used as hydrogen bond donor and for red line CH_3OH is used as hydrogen bond acceptor.

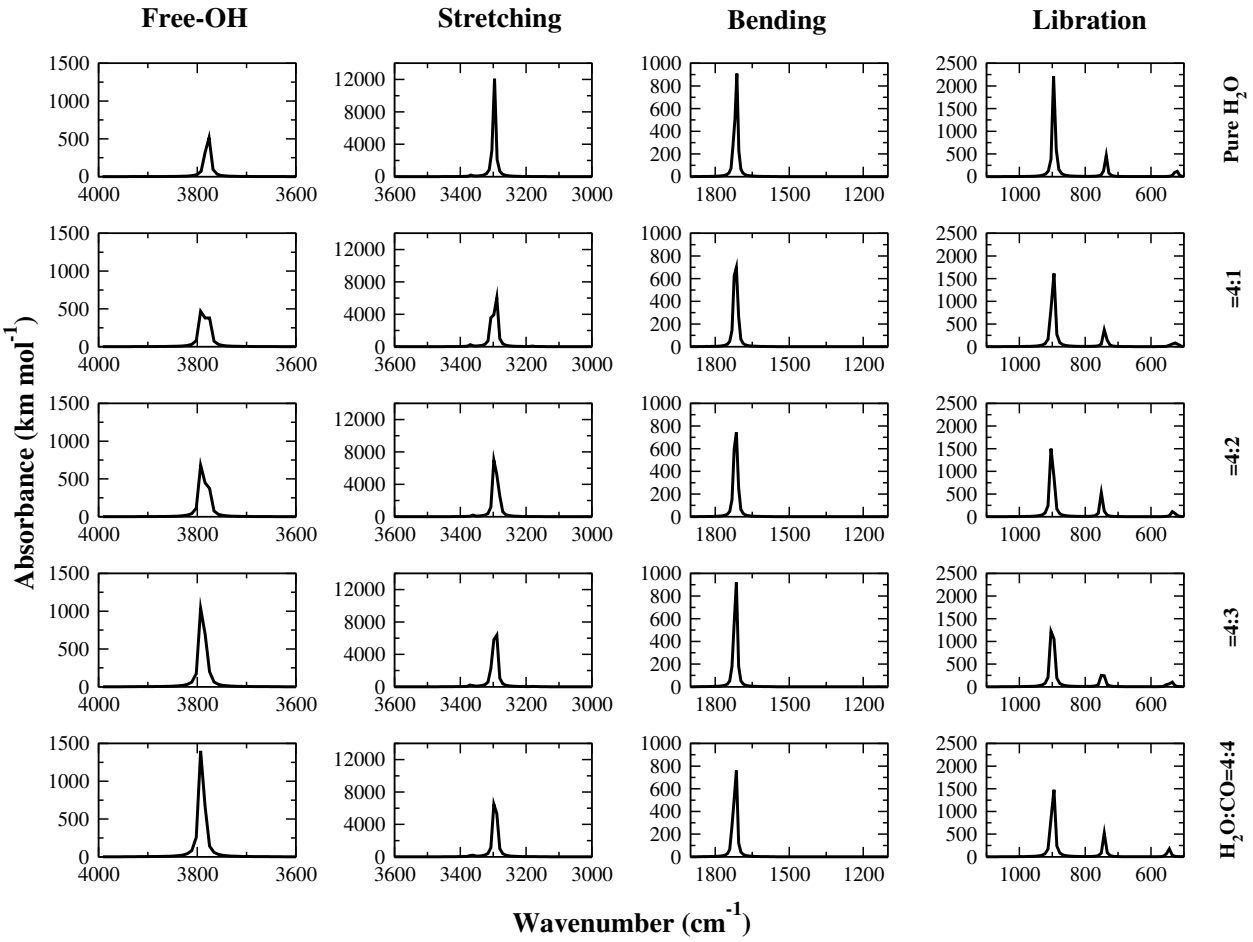

Figure 17: Absorption spectra of the four modes for water ice for the five measured compositions, ranging from pure water ice (top) to 4:4 H_2O-CO mixture (bottom).

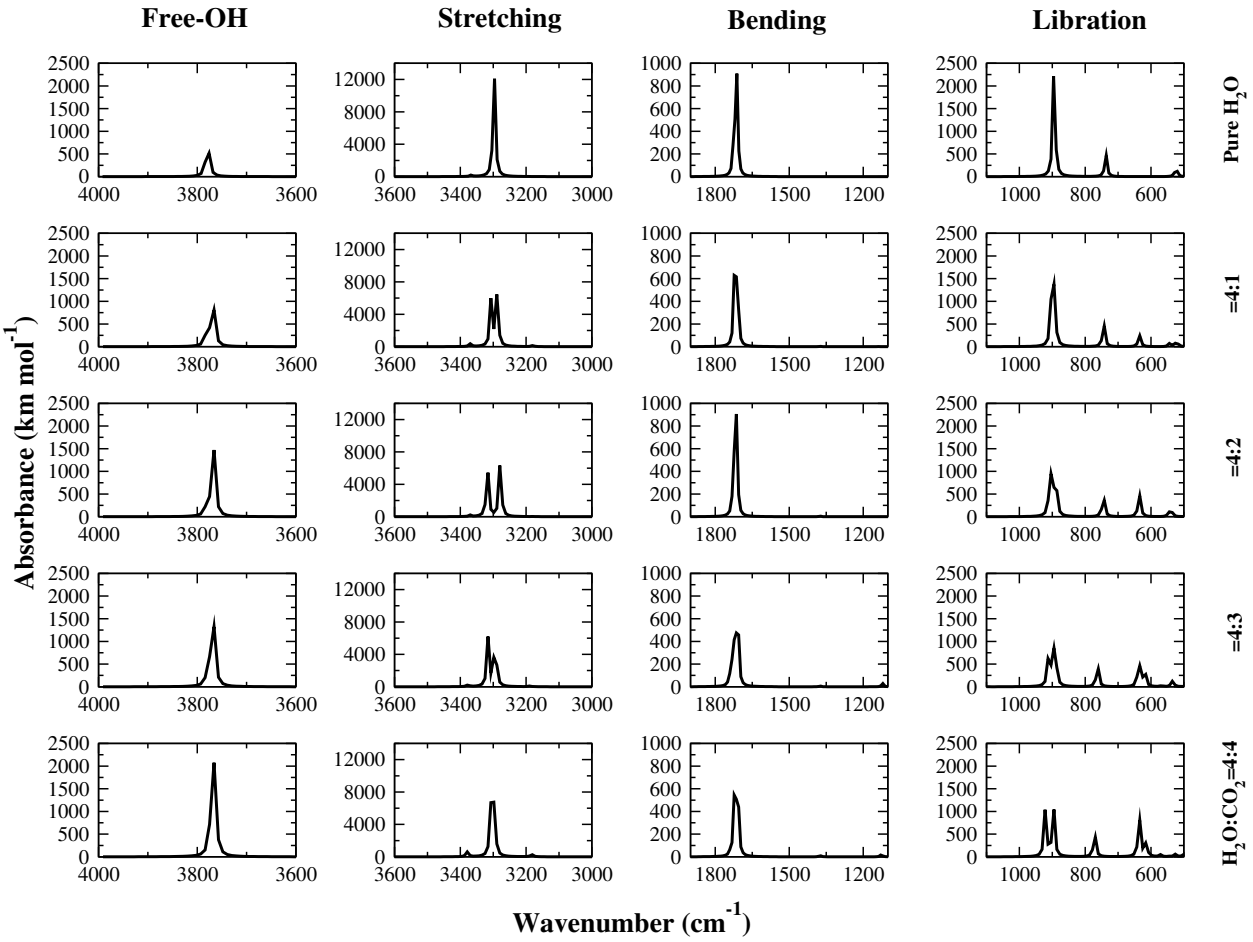

Figure 18: Absorption spectra of the four modes for water ice for the five measured compositions, ranging from pure water ice (top) to 4:4 H_2O-CO_2 mixture (bottom).

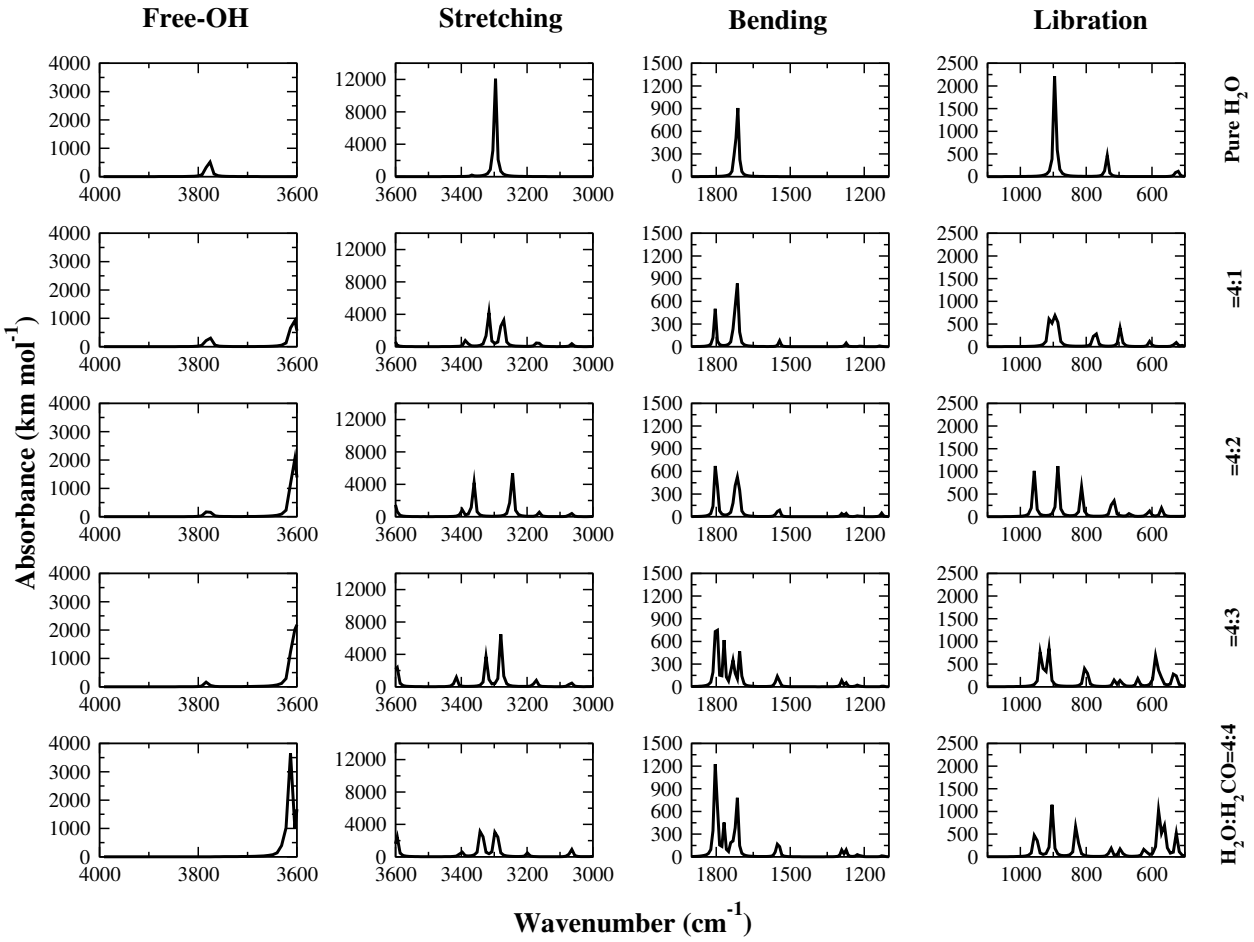

Figure 19: Absorption spectra of the four modes for water ice for the five measured compositions, ranging from pure water ice (top) to 4:4 H_2O-H_2CO mixture (bottom).

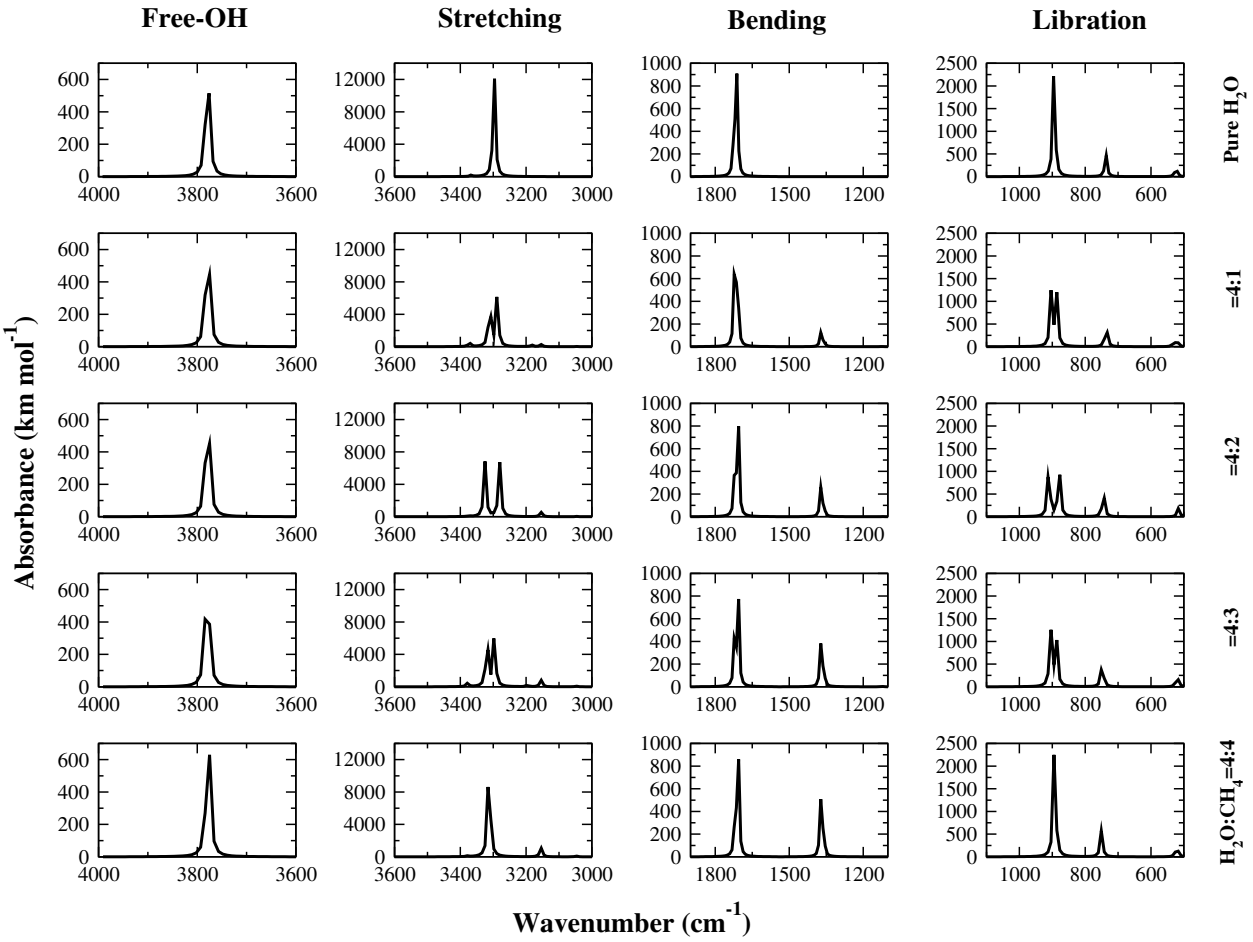

Figure 20: Absorption spectra of the four modes for water ice for the five measured compositions, ranging from pure water ice (top) to 4:4 H_2O-CH_4 mixture (bottom).

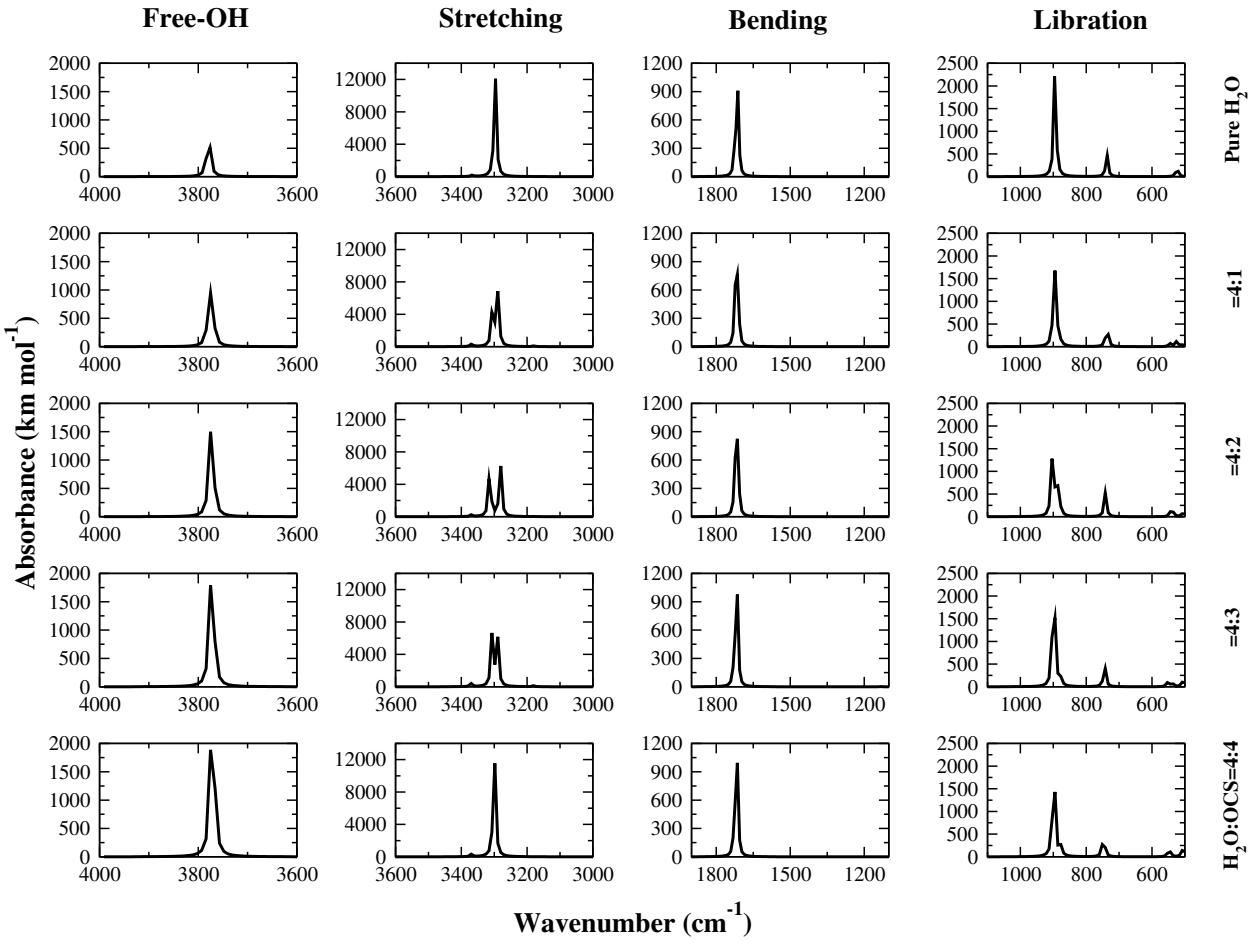

Figure 21: Absorption spectra of the four modes for water ice for the five measured compositions, ranging from pure water ice (top) to 4:4 H_2O-OCS mixture (bottom).

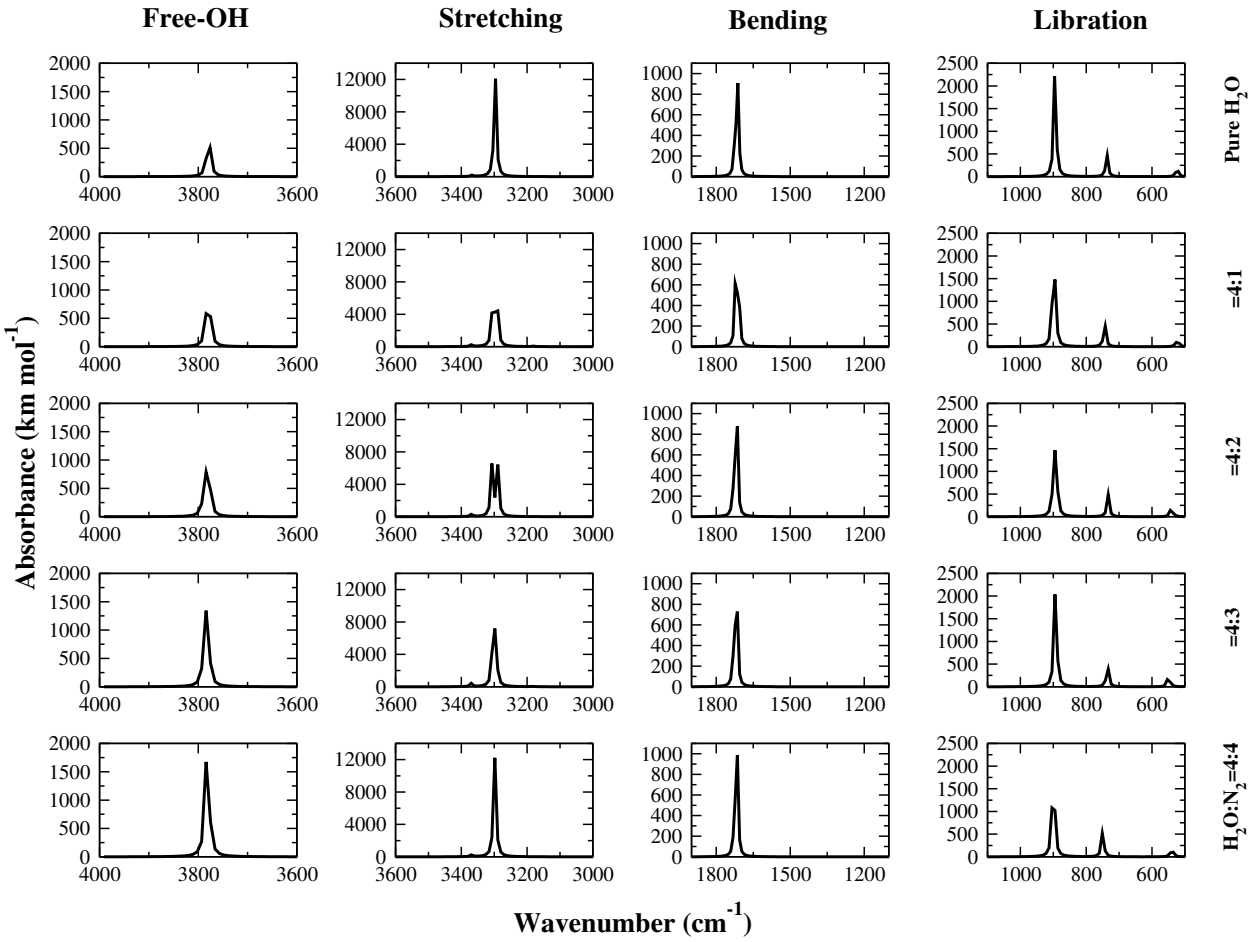

Figure 22: Absorption spectra of the four modes for water ice for the five measured compositions, ranging from pure water ice (top) to 4:4 H_2O-N_2 mixture (bottom).

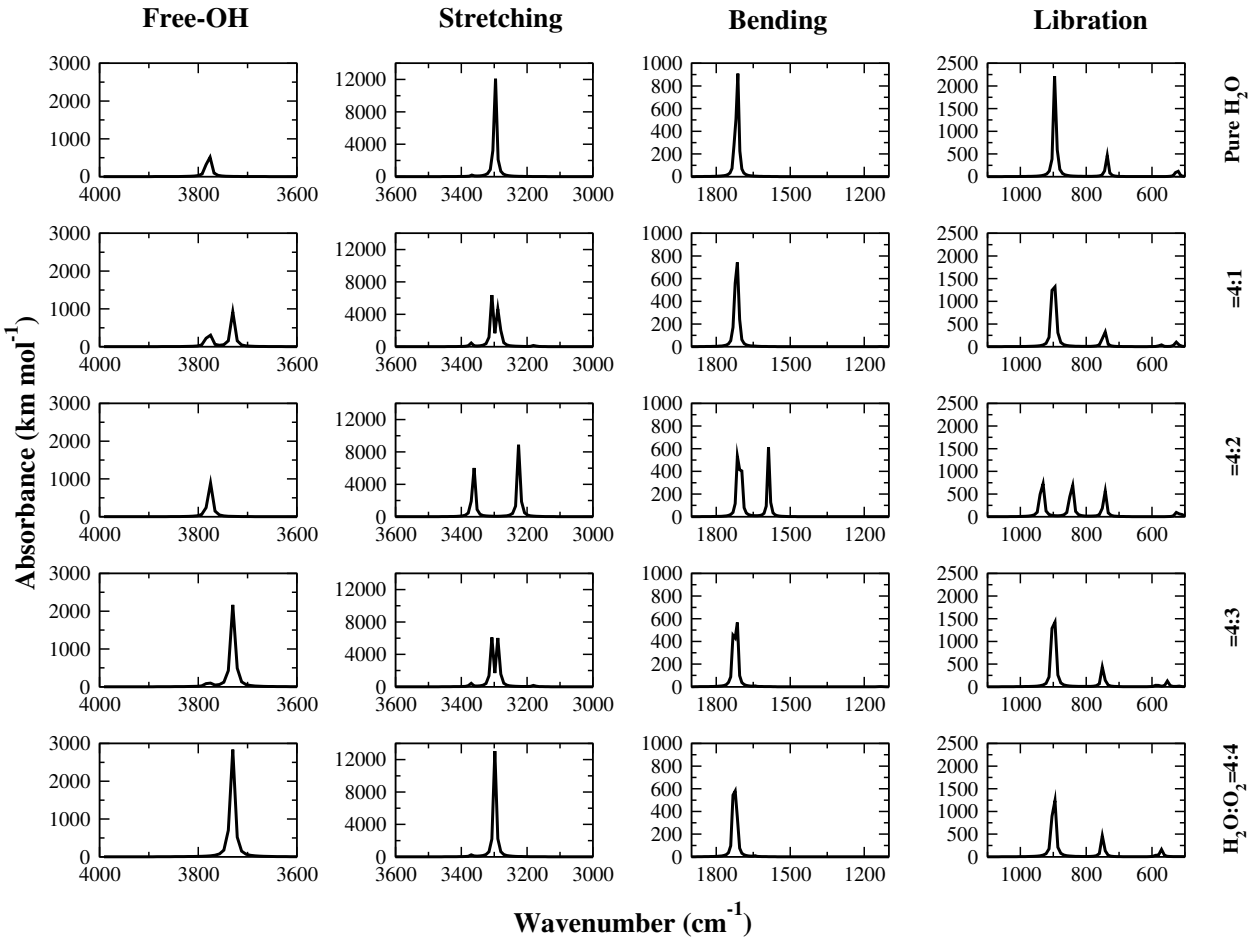

Figure 23: Absorption spectra of the four modes for water ice for the five measured compositions, ranging from pure water ice (top) to 4:4 H_2O-O_2 mixture (bottom).

Table 5: Comparison of band positions and band intensities as obtained by different quantum-chemical methods.

Assignment	$4H_2O$+PCM, B3PLYP/6-31G(d)		$4H_2O$+PCM, B2PLYP/m-aug-cc-pVTZ		$1H_2O$(QM)+$3H_2O$(MM) +PCM, B3PLYP/6-31G(d)		$4H_2O$(QM)+$16H_2O$(MM) +PCM, B3PLYP/6-31G(d)	
	Wavenumber (cm^{-1})	Intensity (km/mol)	Wavenumber (cm^{-1})	Intensity (km/mol)	Wavenumber (cm^{-1})	Intensity (km/mol)	Wavenumber (cm^{-1})	Intensity (km/mol)
1							28.5053	1.6212
2							32.4112	0.3452
3			39.3404	0.0000	39.0097	3.5702	40.5682	1.9422
4	42.31	0.000					42.6937	0.9658
5							45.5125	2.8291
6							47.0457	2.4796
7							51.1545	1.5206
8							53.0040	0.4852
9							57.4113	4.9283
10							58.9090	1.5004
11							62.8440	3.3091
12							64.6577	0.5053
13							67.1132	0.4600
14					70.0478	0.9941	71.0670	1.0092
15							72.1009	5.5430
16							78.5377	1.2279
17							79.5809	2.8592
18			85.5169	4.1241			84.0856	0.3164
19							88.1866	0.5336
20							91.6244	1.1620
21	101.53	0.5953			107.4593	248.8304	95.9146	1.9115
22					114.669	81.5288	131.1634	139.0258
23					134.1712	121.9418	147.4509	6.2284
24							155.1556	1.5936
25							157.0881	12.4196
26							163.8254	4.8492
27							169.5773	3.8618
28							173.1802	11.6779
29							177.8697	22.1882
30							179.4412	3.0508
31							189.5523	12.2882
32							193.8849	18.7990
33							199.5633	30.2086
34			202.1393	0.0000			203.7815	44.7590
35							205.2272	29.8834
36							210.7469	42.9633
37							212.8473	18.5861
38							215.6034	104.3096
39							219.2947	9.1183
40			222.9069	104.7500			221.2358	136.0590
41			22.29069	104.7500			223.7398	14.6743
42							226.9991	92.7095
43							229.4667	11.8754
44			231.0105	94.8938			231.1955	180.5173
45							235.9253	6.3462
46	243.67	0.000	240.0832	0.6734			239.8566	146.4113
47			246.4688	287.8694	251.1220	19.7407	249.2394	2.9212
48			246.4688	287.8694	253.1088	18.8069	254.8166	52.0837
49							260.4354	12.2059
50	277.10	206.9799	274.1815	0.000	270.4875	7.7664	270.0093	13.8498
51	277.10	206.9799			286.0773	10.8931	280.9175	13.8528
52	281.08	0.3532					284.5581	1.3055
53							286.3104	31.7468
54	301.85	0.1654					307.5132	4.0551
55	307.74	298.2083					308.3710	4.8097
56	307.74	298.2083					314.4016	25.2868
57							319.3857	8.4817
58	327.52	0.0000			331.3394	156.5948	330.7679	1.3826
59							334.6995	4.4240
60							347.3954	4.9640
61			398.6011	0.000			387.1876	8.8358

Assignment	$4H_2O$+PCM, B3PLYP/6-31G(d)		$4H_2O$+PCM, B2PLYP/m-aug-cc-pVTZ		$1H_2O$(QM)+$3H_2O$(MM) +PCM, B3PLYP/6-31G(d)		$4H_2O$(QM)+$16H_2O$(MM) +PCM, B3PLYP/6-31G(d)	
	Wavenumber (cm^{-1})	Intensity (km/mol)	Wavenumber (cm^{-1})	Intensity (km/mol)	Wavenumber (cm^{-1})	Intensity (km/mol)	Wavenumber (cm^{-1})	Intensity (km/mol)
62			427.5608	44.2017	417.2017	11.4416	426.8869	78.1914
63							432.7664	47.4011
64			443.1204	79.6160			449.0251	78.8810
65			443.1204	79.6160			455.8202	9.0749
66							458.4089	52.9014
67							461.3395	7.1542
68							468.0311	44.1926
69	473.37	0.000					476.0688	5.2943
70					483.9590	107.2607	483.8486	73.9300
71							500.1090	30.3953
72					502.7496^t	211.3432	500.9839	36.5412
73							508.1366	20.0694
74							512.3840	13.9454
75	523.50	58.1147					532.3995	46.0624
76	523.76	0.9980			539.1224^t	59.4593	535.4481	4.4789
77	523.76	0.9980					543.6866	60.5730
78							545.4049	57.7011
79							557.0745	41.0189
80							560.6706	18.2338
81							581.7986	25.4989
82							585.3805	214.1458
83							588.1325	72.1128
84^t							593.3498	6.1937
85^t							598.2759	204.0196
86^t					620.5928^t	2.9662	620.7530	378.5822
87^t							623.3143	58.9759
88^t							629.3486	219.1103
89^t							639.6399	56.7824
90^t							642.7590	240.6043
91^t							648.3193	65.9335
92^t							658.9772	36.8759
93^t					670.5374^t	209.1029	676.8776	176.4931
94^t							679.7026	594.2500
95^t			683.4168	312.1539			685.0436	47.0063
96^t							690.6345	554.1850
97^t							695.3495	353.6124
98^t							699.7148	156.7689
99^t							704.2320	32.3584
100^t							721.7785	334.5258
101^t	737.11^t	144.3682			734.0061^t	476.6369	725.6449	111.7286
102^t							728.6757	454.3782
103^t							747.1205	168.5362
104^t							753.5614	192.6962
105^t							765.5413	275.9737
106^t			778.3957^t	237.5051			766.1653	425.8765
107^t			778.3957^t	237.5051			772.0067	356.3800
108^t							803.0436	327.2798
109^t							818.6290	277.6746
110^t							839.8062	313.0187
111^t	894.95^t	342.8199			870.1429^t	201.9038	850.6360	671.1597
112^t	894.95^t	342.8199	934.3601^t	0.000			929.4103	415.2180
113^t							955.5738	180.7041
114^t	1127.57^t	0.000					966.2260	55.4464
115^b							1401.1608	328.9992
116^b							1404.9892	279.6521
117^b					1407.2265^b	191.4554	1406.8655	454.2350
118^b							1412.4834	218.9410
119^b							1415.0050	217.1485
120^b							1416.7673	553.3807

Assignment	$4H_2O$+PCM, B3PLYP/6-31G(d)		$4H_2O$+PCM, B2PLYP/m-aug-cc-pVTZ		$1H_2O$(QM)+$3H_2O$(MM) +PCM, B3PLYP/6-31G(d)		$4H_2O$(QM)+$16H_2O$(MM) +PCM, B3PLYP/6-31G(d)	
	Wavenumber (cm^{-1})	Intensity (km/mol)	Wavenumber (cm^{-1})	Intensity (km/mol)	Wavenumber (cm^{-1})	Intensity (km/mol)	Wavenumber (cm^{-1})	Intensity (km/mol)
121^b					1422.8362^b	445.8394	1423.8136	320.7421
122^b							1427.0557	239.2493
123^b							1431.3527	280.4839
124^b							1433.6066	107.3301
125^b							1436.1459	143.6834
126^b							1442.3811	59.3969
127^b					1456.6860^b	64.4541	1456.0330	69.7821
128^b							1465.8850	261.4679
129^b							1481.4184	129.4706
130^b							1490.6689	54.4350
131^b	1711.28^b	251.8157	1630.3695^b	176.7723	1764.1323^b	143.3391	1759.3916	113.0751
132^b	1723.10^b	82.9912	1647.3535^b	74.0296			1781.9431	109.2325
133^b	1723.10^b	82.9911	1647.3536^b	74.0296			1805.1440	185.2649
134^b	1741.00^b	0.0000	1672.6698^b	0.000			1821.5031	81.3961
135^s	3182.21^s	0.0000					3277.1620	1061.3522
136^s	3297.07^s	1871.6907					3379.4017	1450.1515
137^s	3297.07^s	1871.6907	3411.5900^s	0.000	3399.8219^s	161.5281	3415.3773	260.6407
138^s	3366.39^s	50.2255	3477.3996^s	1793.2478			3441.1055	54.0971
139^s			3477.3996^s	1793.2478			3501.0930	137.3189
140^s							3510.2084	280.1448
141^s							3515.4119	164.7163
142^s			3522.3300^s	2.0149			3527.1563	98.4213
143^s					3533.5836^s	119.6470	3532.0223	374.1860
144^s							3535.9755	331.7897
145^s							3539.5696	667.4359
146^s							3541.9090	42.2047
147^s							3546.9082	185.0747
148^s							3549.9374	209.7596
149^s							3555.5498	189.4891
150^s							3558.8959	76.1871
151^s					3561.1437^s	374.8984	3563.2840	189.8014
152^s							3568.4433	217.3753
153^s							3575.4761	97.1563
154^s							3576.5391	86.9267
155^s					3579.9423^s	110.7922	3579.7822	19.6952
156^s							3589.8658	38.6004
157^s							3590.2134	57.5165
158^s							3603.0421	149.2000
159^s							3618.1897	266.3486
160^s							3620.8200	224.9253
161^s							3622.0658	233.3283
162^s							3623.0520	397.9328
163^s							3624.0959	35.3011
164^s							3626.6346	276.1415
165^s							3630.3037	955.2942
166^s							3631.8424	16.4537
167^s							3633.8572	248.7481
168^f					3643.1130^f	84.3280	3646.1348	108.4691
169^f					3647.6874^f	450.2363	3650.9996	175.2420
170^f					3651.3875^f	90.6885	3652.3329	128.0414
171^f	3778.38^f	126.4545	3864.6871^f	144.7620			3652.8838	205.0487
172^f	3779.79^f	52.8022	3865.9912^f	138.6232			3653.3844	33.2033
173^f	3779.79^f	52.8022	3865.9912^f	138.6232			3653.8800	205.2072
174^f	3781.36^f	0.0000	3867.1847^f	0.0000	3797.0095^f	37.5965	3654.0193	86.2440

Notes: ^{t}OH torsion; ^{b}OH scissoring; ^{s}OH stretching; ^{f}free OH. For the conversion of km/mol to cm molecule^{-1}, intensity values need to multiply by a factor 1.6603×10^{-19}.

Table 6: Frequencies, integral absorbance coefficients, and normal modes of vibration of H_2O-X (X = HCOOH, NH_3, CH_3OH, CO, CO_2, H_2CO, CH_4, OCS, N_2, and O_2)

H_2O : X	**Frequency at peak in cm^{-1} (μm)**	**Integral absorbance coefficient in cm $molecule^{-1}$**	**Modes of vibration**
		HCOOH	
1:0.25	875.47 (11.42)	5.98×10^{-17}	OH torsion
	1698.42 (5.89)	5.24×10^{-17}	H_2O scissoring
	3326.84 (3.00)	1.88×10^{-16}	OH stretching
	3635.02 (2.75)	4.11×10^{-17}	free OH
1:0.50	859.72 (11.63)	6.18×10^{-17}	OH torsion
	1696.3 (5.90)	5.37×10^{-17}	H_2O scissoring
	3341.67 (2.99)	2.08×10^{-16}	OH stretching
	3632.99 (2.75)	4.19×10^{-17}	free OH
1:0.75	878.28 (11.38)	4.91×10^{-17}	OH torsion
	1688.62 (5.92)	6.27×10^{-17}	H_2O scissoring
	3260.11 (3.07)	2.46×10^{-16}	OH stretching
	3611.81 (2.77)	6.46×10^{-17}	free OH
1:1.00	747.49 (13.38)	9.21×10^{-17}	OH torsion
	1685.24 (5.93)	7.56×10^{-17}	H_2O scissoring
	3343.53 (2.99)	2.08×10^{-16}	OH stretching
	3608.22 (2.77)	7.15×10^{-17}	free OH
		NH_3	
1:0.25	886.69 (11.28)	7.31×10^{-17}	OH torsion
	1717.36 (5.82)	3.58×10^{-17}	H_2O scissoring
	3055.07 (3.27)	2.20×10^{-16}	OH stretching
	3778.71 (2.65)	1.16×10^{-17}	free OH
1:0.50	877.63 (11.39)	8.92×10^{-17}	OH torsion
	1725.39 (5.80)	3.28×10^{-17}	H_2O scissoring
	3127.37 (3.20)	4.38×10^{-16}	OH stretching
	3737.41 (2.65)	7.02×10^{-18}	free OH
1:0.75	859.21 (11.64)	4.99×10^{-17}	OH torsion
	1730.52 (5.78)	2.47×10^{-17}	H_2O scissoring
	3264.44 (3.06)	4.27×10^{-16}	OH stretching
	3777.53 (2.65)	5.89×10^{-18}	free OH
1:1.00	938.38 (10.66)	9.35×10^{-17}	OH torsion
	1751.53 (5.71)	4.43×10^{-17}	H_2O scissoring
	3270.01 (3.06)	4.90×10^{-16}	OH stretching
	–	–	free OH
		CH_3OH	
1:0.25	751.68 (13.30)	5.60×10^{-17}	OH torsion
	1703.98 (5.87)	3.85×10^{-17}	H_2O scissoring
	3252.5 (3.07)	2.33×10^{-16}	OH stretching
	3774.67 (2.65)	1.73×10^{-17}	free OH
1:0.50	719.11 (13.91)	7.67×10^{-17}	OH torsion
	1654.59 (6.04)	3.62×10^{-17}	H_2O scissoring
	3207.15 (3.12)	4.57×10^{-16}	OH stretching
	3843.18 (2.60)	2.26×10^{-17}	free OH
1:0.75	702.71 (14.23)	5.49×10^{-17}	OH torsion
	1690.03 (5.92)	2.92×10^{-17}	H_2O scissoring
	3351.12 (2.96)	2.25×10^{-16}	OH stretching
	3783.4 (2.64)	1.72×10^{-17}	free OH
1:1.00	906.29 (11.03)	6.61×10^{-17}	OH torsion
	1693.39 (5.90)	2.96×10^{-17}	H_2O scissoring
	3295.67 (3.03)	3.97×10^{-16}	OH stretching
	3774.54 (2.65)	2.03×10^{-17}	free OH

H_2O : X	**Frequency at peak in cm^{-1} (μm)**	**Integral absorbance coefficient in cm $molecule^{-1}$**	**Modes of vibration**
		CO	
1:0.25	895.46 (11.17)	5.70×10^{-17}	OH torsion
	1711.46 (5.84)	4.14×10^{-17}	H_2O scissoring
	3290.66 (3.04)	3.14×10^{-16}	OH stretching
	3791.25 (2.64)	2.39×10^{-17}	free OH
1:0.50	898.71 (11.13)	5.64×10^{-17}	OH torsion
	1711.73 (5.84)	4.19×10^{-17}	H_2O scissoring
	3285.68 (3.04)	3.22×10^{-16}	OH stretching
	3791.07 (2.64)	2.42×10^{-17}	free OH
1:0.75	898.22 (11.13)	5.71×10^{-17}	OH torsion
	1713.47 (5.84)	4.18×10^{-17}	H_2O scissoring
	3290.55 (3.04)	3.16×10^{-16}	OH stretching
	3789.19 (2.64)	4.93×10^{-17}	free OH
1:1.00	899.44 (11.12)	5.89×10^{-17}	OH torsion
	1715.94 (5.83)	4.22×10^{-17}	H_2O scissoring
	3293.09 (3.04)	3.13×10^{-16}	OH stretching
	3789.31 (2.64)	6.92×10^{-17}	free OH
		CO_2	
1:0.25	893.79 (11.19)	5.63×10^{-17}	OH torsion
	1710.62 (5.84)	4.23×10^{-17}	H_2O scissoring
	3288.08 (3.04)	3.10×10^{-16}	OH stretching
	3766.88 (2.65)	3.85×10^{-17}	free OH
1:0.50	890.45 (11.23)	5.72×10^{-17}	OH torsion
	1713.11 (5.84)	4.22×10^{-17}	H_2O scissoring
	3278.84 (3.05)	3.26×10^{-16}	OH stretching
	3767.04 (2.65)	4.21×10^{-17}	free OH
1:0.75	891.90 (11.21)	5.98×10^{-17}	OH torsion
	1709.11 (5.85)	4.20×10^{-17}	H_2O scissoring
	3294.04 (3.04)	3.17×10^{-16}	OH stretching
	3766.76 (2.65)	5.31×10^{-17}	free OH
1:1.00	896.53 (11.15)	5.61×10^{-17}	OH torsion
	1709.45 (5.85)	4.41×10^{-17}	H_2O scissoring
	3296.79 (3.03)	3.05×10^{-16}	OH stretching
	3765.50 (2.66)	7.28×10^{-17}	free OH
		H_2CO	
1:0.25	890.85 (11.22)	6.00×10^{-17}	OH torsion
	1712.86 (5.84)	3.97×10^{-17}	H_2O scissoring
	3274.97 (3.05)	3.06×10^{-16}	OH stretching
	3607.83 (2.77)	8.46×10^{-17}	free OH
1:0.50	886.56 (11.28)	5.44×10^{-17}	OH torsion
	1710.12 (5.85)	4.17×10^{-17}	H_2O scissoring
	3246.10 (3.08)	3.27×10^{-16}	OH stretching
	3601.67 (2.78)	9.12×10^{-17}	free OH
1:0.75	937.07 (10.67)	5.41×10^{-17}	OH torsion
	1767.86 (5.66)	2.81×10^{-17}	H_2O scissoring
	3279.19 (3.05)	3.23×10^{-16}	OH stretching
	3607.45 (2.77)	1.35×10^{-17}	free OH
1:1.00	904.32 (11.06)	5.51×10^{-17}	OH torsion
	1713.74 (5.84)	3.51×10^{-17}	H_2O scissoring
	3338.99 (2.99)	2.96×10^{-16}	OH stretching
	3612.36 (2.77)	9.67×10^{-17}	free OH

H_2O : X	**Frequency at peak in cm^{-1} (μm)**	**Integral absorbance coefficient in cm $molecule^{-1}$**	**Modes of vibration**
		CH_4	
1:0.25	903.11 (11.07)	5.96×10^{-17}	OH torsion
	1710.29 (5.85)	4.14×10^{-17}	H_2O scissoring
	3287.91 (3.04)	3.06×10^{-16}	OH stretching
	3777.98 (2.65)	2.03×10^{-17}	free OH
1:0.50	910.32 (10.98)	5.97×10^{-17}	OH torsion
	1706.49 (5.86)	4.14×10^{-17}	H_2O scissoring
	3280.67 (3.05)	3.30×10^{-16}	OH stretching
	3778.16 (2.65)	2.16×10^{-17}	free OH
1:0.75	905.03 (11.05)	6.05×10^{-17}	OH torsion
	1706.58 (5.86)	4.10×10^{-17}	H_2O scissoring
	3296.35 (3.03)	3.22×10^{-16}	OH stretching
	3778.86 (2.65)	2.18×10^{-17}	free OH
1:1.00	893.41 (11.19)	6.23×10^{-17}	OH torsion
	1705.91 (5.86)	4.11×10^{-17}	H_2O scissoring
	3312.78 (3.02)	3.41×10^{-16}	OH stretching
	3777.04 (2.65)	2.40×10^{-17}	free OH
		OCS	
1:0.25	897.72 (11.14)	5.74×10^{-17}	OH torsion
	1711.96 (5.84)	4.11×10^{-17}	H_2O scissoring
	3288.8 (3.04)	3.10×10^{-16}	OH stretching
	3772.38 (2.65)	4.82×10^{-17}	free OH
1:0.50	889.91 (11.24)	5.80×10^{-17}	OH torsion
	1712.15 (5.84)	4.30×10^{-17}	H_2O scissoring
	3281.28 (3.05)	3.27×10^{-16}	OH stretching
	3772.57 (2.65)	6.60×10^{-17}	free OH
1:0.75	901.72 (11.09)	5.77×10^{-17}	OH torsion
	1713.88 (5.83)	4.40×10^{-17}	H_2O scissoring
	3290.61 (3.04)	3.26×10^{-16}	OH stretching
	3771.53 (2.65)	9.02×10^{-17}	free OH
1:1.00	897.75 (11.14)	5.75×10^{-17}	OH torsion
	1713.97 (5.83)	4.47×10^{-17}	H_2O scissoring
	3299.75 (3.03)	3.29×10^{-16}	OH stretching
	3770.63 (2.65)	1.11×10^{-16}	free OH
		N_2	
1:0.25	894.31 (11.18)	5.63×10^{-17}	OH torsion
	1709.81 (5.85)	4.16×10^{-17}	H_2O scissoring
	3292.23 (3.04)	3.16×10^{-16}	OH stretching
	3778.08 (2.65)	2.34×10^{-17}	free OH
1:0.50	889.34 (11.24)	5.98×10^{-17}	OH torsion
	1716.33 (5.83)	4.54×10^{-17}	H_2O scissoring
	3290.41 (3.04)	3.10×10^{-16}	OH stretching
	3778.76 (2.65)	2.36×10^{-17}	free OH
1:0.75	892.07 (11.21)	5.98×10^{-17}	OH torsion
	1716.67 (5.82)	4.69×10^{-17}	H_2O scissoring
	3295.86 (3.03)	3.05×10^{-16}	OH stretching
	3784.28 (2.64)	5.14×10^{-17}	free OH
1:1.00	899.90 (11.11)	5.73×10^{-17}	OH torsion
	1714.47 (5.83)	4.52×10^{-17}	H_2O scissoring
	3297.32 (3.03)	3.15×10^{-16}	OH stretching
	3780.99 (2.64)	7.59×10^{-17}	free OH

H_2O : X	**Frequency at peak in cm^{-1} (μm)**	**Integral absorbance coefficient in cm $molecule^{-1}$**	**Modes of vibration**
		O_2	
1:0.25	893.78 (11.19)	5.65×10^{-17}	OH torsion
	1711.86 (5.84)	4.11×10^{-17}	H_2O scissoring
	3286.24 (3.04)	3.10×10^{-16}	OH stretching
	3729.93 (2.68)	4.41×10^{-17}	free OH
1:0.50	934.71 (10.70)	6.49×10^{-17}	OH torsion
	1700.17 (5.88)	3.78×10^{-17}	H_2O scissoring
	3225.04 (3.10)	4.51×10^{-16}	OH stretching
	3774.84 (2.65)	2.77×10^{-17}	free OH
1:0.75	892.96 (11.20)	5.75×10^{-17}	OH torsion
	1717.35 (5.82)	4.04×10^{-17}	H_2O scissoring
	3286.59 (3.04)	3.12×10^{-16}	OH stretching
	3729.19 (2.68)	8.72×10^{-17}	free OH
1:1.00	900.52 (11.10)	5.67×10^{-17}	OH torsion
	1718.90 (5.82)	4.18×10^{-17}	H_2O scissoring
	3299.52 (3.03)	3.19×10^{-16}	OH stretching
	3727.75 (2.68)	1.08×10^{-16}	free OH